HEAT TRANSPORT IN GRAPHENE

Serap Yiğen

A thesis
in
The Department
of
Physics

Presented in Partial Fulfillment of the Requirements
For the Degree of Master of Science (Physics)
Concordia University
Montréal, Québec, Canada

December 2010

CONCORDIA UNIVERSITY
School of Graduate Studies

This is to certify that the thesis prepared

By: **Serap Yiğen**
Entitled: **Heat Transport in Graphene**

and submitted in partial fulfillment of the requirements for the degree of

Master of Science (Physics)

complies with the regulations of this University and meets the accepted standards with respect to originality and quality.

Signed by the final examining commitee:

______________________________ Chair
Dr. Truong Vo-Van
______________________________ Examiner
Dr. Laszlo Kalman
______________________________ Examiner
Dr. Valter Zazubovich
______________________________ Supervisor
Dr. Alexandre Champagne

Approved by ______________________________
Dr. Truong Vo-Van
Chair of Department or Graduate Program Director

________ 20 ____ ____________________
Dr. Brian Lewis
Dean of Faculty

Abstract

Heat Transport in Graphene

Serap Yiğen

Heat transport studies are a powerful tool to obtain information about both the phononic and electronic properties of materials. Graphene is a two-dimensional crystal (1-atom thick) where electrons behave relativistically, and which has tremendous potential for short-term technological applications. We measure the heat conductivity of graphene, and aim to gather fundamental information about its phonon modes and their coupling to its Dirac fermions (electrons or holes). Our measurements can also assess the potential of graphene for technological applications such as heat management in nanodevices.

We report the first detailed measurements of heat conductivity, κ, and electron mobility, of graphene versus temperature (6K - 350K) and charge density. We have fabricated suspended graphene devices. Our suspended devices prevent any undesired heat leakage and allow a simple modeling of the heat transport. We use these graphene devices as their own heat sources (Joule heating) and thermometers (resistivity) to measure their heat conductivity. We observe that thermal conductivity varies by 3 orders of magnitude as a function of temperature, indicating phonon heat transport, and by more than an order of magnitude as a function of charge density, suggesting that electron-phonon coupling is important. We observed κ up to 1500 $W/m.K$.

Acknowledgments

I would like to express my deepest gratitude to my supervisor, Dr. Alexandre Champagne for his continuous support, motivation and patience throughout this study. His wide knowledge, enthusiasm in research and guidance helped me a lot to overcome many problems and to accomplish this project. I am grateful to have the chance of being trained as a future scientist under his supervision.

I would like to thank my colleagues, Joshua Island and Vahid Tayari for their support and help. It was pleasure and also fun to work with them in the lab. I wish you guys a great future and career.

I am thankful for the support and encouragements of Ismail Turan and Alper Hayreter. I was lucky to have them here when I first stepped into my new life in Montreal.

I am grateful to Dr. Barry Frank and his sweet wife Donnie Frank for being like a family to me when I just arrived in Montreal. There is no way to thank them for their help and understanding.

I would like to express my sincere thanks to Dr. Durmus A. Demir. I am thankful for his support and motivation throughout my undergraduate studies. I am lucky to have had the chance to meet him.

My special thanks go to my dear friend Beste Korutlu for her presence, great friendship and support. It gave me great confidence and happiness to have her help whenever I needed. I had and am still having great and fun times with her. Thanks to all of my friends who supported and helped me during my studies.

Last but foremost, I would like to thank my parents for their endless love and encouragements. Without their presence in my life, this accomplishment would never have been. I am grateful to have such wonderful parents.

Contents

List of Figures **viii**

List of Tables **xii**

1 Introduction **1**

2 Graphene Basics and Heat Transport Model **4**

2.1 Graphene 4

2.2 Heat Transport Model for Graphene 11

2.2.1 Joule-Heating Technique 11

2.2.2 Self-Heating Technique 12

3 Fabrication of Suspended Graphene Devices and Instrumentation **23**

3.1 Sample Fabrication 24

3.1.1 Reactive Ion Etching (RIE) 24

3.1.2 Photolithography 26

3.1.3 Electron Beam Evaporation 27

3.1.4 Graphene Deposition 28

3.1.5 Electron Beam Lithography 30
3.1.5.1 Devices for Self-heating: 32
3.1.5.2 Devices for Joule-heating: 33
3.1.6 Suspension of Graphene Crystals 33
3.2 Instrumentation 34

4 Measurements and Data analysis 38

4.1 Electron Transport in Graphene 39
4.1.1 Measurements 39
4.1.2 Data Analysis 40
4.2 Heat Transport in Graphene 42
4.2.1 Measurements 42
4.2.2 Data Analysis 45
4.2.3 Discussion 50

5 Conclusion 54

List of Figures

2.1 Graphene is the basis of all graphitic forms [3]. 5

2.2 **a.** Energy band structure of graphene [7]. **b.** Honeycomb lattice and corresponding First Brillouin zone [6]. 6

2.3 Quantum Hall Effect in graphene [3]. 9

2.4 Phonon dispersions along high symmetry directions in the first Brillouin zone of graphene [27]. 10

2.5 Cartoon of the device design for the Joule-heating technique. 12

2.6 Cartoon of a self-heating device 13

2.7 Boundary conditions for Self-heating model 14

2.8 $\frac{T}{T_0}$ for $\rho_{ref} = 5000\ \Omega$ and $\kappa = 3000\ Wm^{-1}K^{-1}$. **a.** For $I = 1\ \mu A$ at contact temperatures of $T_0 = 1.5$, 10 and 100 K. **b.** For $I = 10\ \mu A$ **c.** $I = 100\ \mu A$ **d.** $I = 1000\ \mu A$. 16

2.9 $\frac{T}{T_0}$ for $\rho_{ref} = 500\ \Omega$ and $\kappa = 3000\ Wm^{-1}K^{-1}$ **a.** For $I = 1\ \mu A$ at contact temperatures of $T_0 = 1.5$, 10 and 100 K. **b.** For $I = 10\ \mu A$ **c.** $I = 100\ \mu A$ **d.** $I = 1000\ \mu A$. 19

2.10 $\frac{T}{T_0}$ for $\rho_{ref} = 5000\ \Omega$ and $\kappa = 1\ Wm^{-1}K^{-1}$. **a.** For $I = 1\ \mu A$ at contact temperatures of $T_0 = 1.5$, 10 and 100 K. **b.** For $I = 10\ \mu A$ **c.** $I = 100\ \mu A$. 20

3.1 Flow-chart diagram of the fabrication of our graphene devices. 24

3.2 Reactive ion etching (RIE). RIE removes the SiO_2 from the backside of the wafer. 25

3.3 Mask Pattern and Alignment Marks. Cartoon of a 4-inch wafer with 4 × 4 mm dies with alignment marks. The inset is a zoom-in on a portion of one die and shows the dimensions of the alignment marks. 27

3.4 Optical image of a chip with alignment marks. 28

3.5 One layer and a few layers of graphene under an optical microscope with 1000x magnification. 29

3.6 Electron-Beam lithography procedure. **a.** Optical image of a graphene flake. **b.** A grid is defined on the image to locate the flake, and the contacts are drawn by AUTOCAD. **c.** Optical image after developing e-beam pattern. **d.** Optical image after metal lift-off. 31

3.7 Optical images of self-heating devices. 32

3.8 Optical image of a joule-heating device. 33

3.9 SEM image of a suspended graphene device. 34

3.10 Measurement set-up an instrumentation. **a.** Optical image of a device after wire-bonding showing the large (200 × 200 μm) contact pads at the end of the source and drain electrodes. **b.** Sample mount of the cryostat with a mounted chip carrier. **c.** Cryostat connected with turbo-pump and electronics. 36

3.11 The graphical interface of our home-made software for data acquisition. 36

3.12 Measurement circuit. The Data Acquisition Card (DAQ) applies voltages and reads the output current from the pre-amplifier. There is gate voltage source (Keithley) which tunes the carrier density. The entire circuit is controlled by a PC. 37

4.1 I versus V_{bias} at different V_{gate}. 39

4.2 I versus V_{gate}, V_{bias}=5 mV, T=300 K. 40

4.3 Current versus bias voltage at T=79 K. 43

4.4 Resistance versus temperature calibration curve between 77 K and 300 K. 44

4.5 Large bias voltage sweep to heat up the graphene and measure κ. . . 44

4.6 Resistance versus temperature calibration curve. 45

4.7 I vs V_{gate} before and after annealing. 48

4.8 κ vs T before and after annealing. 48

4.9 Thermal conductivity versus temperature at $V_{gate} = -2.5\ V$, which corresponds to $n_{carrier} \simeq 0.2 \times 10^{11}\ cm^{-2}$. 49

4.10 Thermal conductivity versus charge carrier density at $T = 350\ K$. . . 50

4.11 Thermal conductivity versus T for different crystal lengths [31]. . . . 51

List of Tables

2.1 $\Delta T = T_{middle} - T_0$ for $\rho_{ref} = 5000\ \Omega$ and $\kappa = 3000\ Wm^{-1}K^{-1}$ 17

2.2 $\Delta T = T_{middle} - T_0$ for $\rho_{ref} = 500\ \Omega$ and $\kappa = 3000\ Wm^{-1}K^{-1}$ 18

2.3 $\Delta T = T_{middle} - T_0$ for $\rho_{ref} = 5000\ \Omega$ and $\kappa = 1\ Wm^{-1}K^{-1}$ 21

Chapter 1

Introduction

Heat transport study is a powerful tool to obtain information about both phononic and electronic properties of materials, since the thermal conductivity of materials has contributions from both electrons and phonons. Moreover, it also contains information about the interactions between phonons and electrons. In this project we designed and developed an experimental procedure to make precise heat conductivity, κ, measurements in graphene. We present κ data as a function of temperature, T, and charge carrier density, n.

Graphene is a monolayer of carbon atoms packed in a hexagonal lattice. It was first isolated by A. Geim and K. Novoselov in 2004 from graphite using scotch tape to cleave atomic planes. This discovery lead them to a Nobel Prize in Physics in 2010. After its discovery, graphene had an enormous impact on many research areas, not only in condensed matter but also in engineering and chemistry. Thousands of graphene papers are published every year and as its unusual properties are being revealed, it leads to more potential future applications. One of the things that makes graphene unique is its linear band structure which makes its charge carriers behave like relativistic particles described by Dirac's equation. In addition to its electronic properties, its phononic properties are different than other 2D systems. Since it is a two-dimensional material free to move in a three-dimensional world, it has out-of-plane phonon modes. To explore these electronic and phononic properties, we developed a method to measure the heat conductivity of graphene.

We fabricated suspended graphene devices which prevent undesired heat leakage to the substrate to provide precise measurements. We developed a self-heating technique in which we flow a current to heat up graphene and use the resistivity of the graphene crystal as a thermometer to measure its temperature. Thanks to our device design we can measure κ at different charge carrier densities and at different temperatures. We annealed our samples to see the effect of impurities on thermal conductivity. We see a strong dependence of κ on temperature and impurity concentration. We compare our results with theory and previous experiments and find that our results are consistent with literature.

In this thesis, we report detailed measurements of the thermal conductivity of graphene. In chapter 2, we briefly review the physics of graphene and present the heat transport model we built. In chapter 3, we explain the fabrication techniques we used to make our devices, and describe the measurement set-up we used for data acquisition. In chapter 4, we show how we extract thermal conductivity from our model and present our results.

Chapter 2

Graphene Basics and Heat Transport Model

In this chapter we present a theoretical background for heat transport in graphene before introducing our experimental work in chapter 3. First, we give a brief overview of graphene's electrical and mechanical properties and in the following section we present the heat transport model we built to analyze our data and extract thermal conductivity.

2.1 Graphene

Graphene is a monolayer of carbon atoms arranged in a honeycomb lattice and is the 2D building material for all other graphitic materials such as fullerenes (0D), carbon nanotubes (1D) and graphite (3D) (see Fig. 2.1). Graphene had been studied only theoretically before 2004, since it was not expected that such a 2D structure could be thermodynamically stable and it had never been observed experimentally. The story changed in 2004, when A. K Geim *et al.* at the University of Manchester [1, 2] could isolate graphene layers on a silicon substrate and start acquiring data which revealed the unusual properties of graphene. In this section we will briefly review some of the physical properties which make graphene special for both fundamental physics research and applications in electronics.

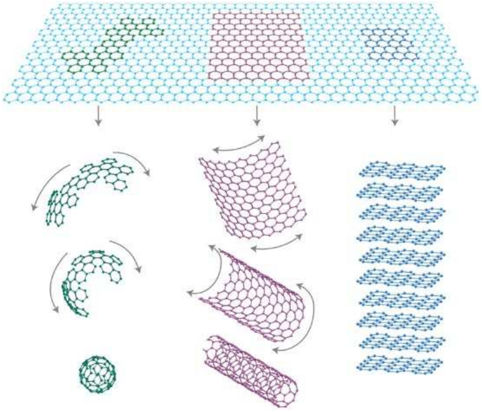

Figure 2.1: Graphene is the basis of all graphitic forms [3].

After the experimental discovery of graphene, its exceptional mechanical and electronic properties attracted enormous attention. These properties stem from its chemical bonding and lattice structure. Each carbon atom in graphene binds to 3 nearest neighbors (see Fig. 2.2b) and is sp^2 hybridized. The three sp^2 orbitals are generated by one $2s$ orbital hybridized with the $2p_x$ and $2p_y$ orbitals in each carbon atom. These orbitals form strong σ bonds with the neighboring carbon atoms. The σ bonds are parallel to the plane of graphene and are responsible for the mechanical strength of the sheet. Experiments on the mechanical properties of graphene have proven that it is the strongest material ever measured with a Young's modulus of 0.5 TPa [4, 5]. The $2p_z$ orbitals which are not sp^2 hybridized and each have one electron which forms π bonds between nearest neighbors and leads to delocalized π bands. These half-filled π bands give rise to the conduction and valance electronic bands in graphene. These energy bands play an important role in the electron transport properties of graphene. Their dispersion is linear, and the valence and conduction bands meet at a point called Dirac Point or Neutrality Point (see Fig. 2.2a.). Because of this structure, graphene is called a zero band gap semiconductor.

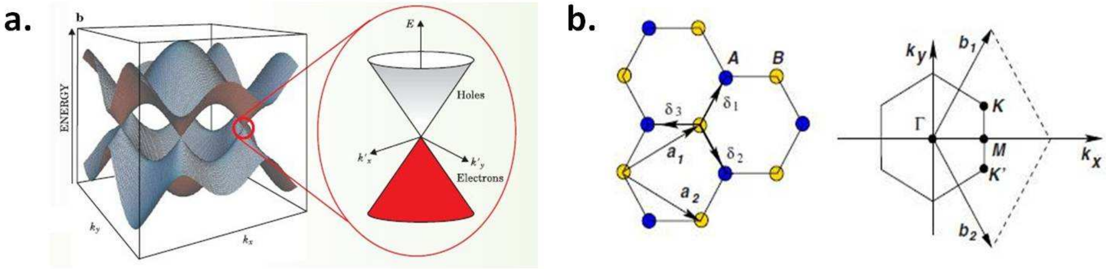

Figure 2.2: **a.** Energy band structure of graphene [7]. **b.** Honeycomb lattice and corresponding First Brillouin zone [6].

The lattice structure of graphene can be thought of as a hexagonal lattice with a basis of two atoms per unit cell with the lattice vectors

$$a_1 = \frac{a}{2}(3, \sqrt{3}) \qquad , \qquad a_2 = \frac{a}{2}(3, -\sqrt{3}) \tag{2.1}$$

The Dirac points are located at K and $K^{'}$ in the reciprocal space are (see Fig. 2.2b.)

$$K = (\frac{2\pi}{3a}, \frac{2\pi}{3\sqrt{3}a}) \qquad , \qquad K^{'} = (\frac{2\pi}{3a}, -\frac{2\pi}{3\sqrt{3}a}) \tag{2.2}$$

The energy dispersion relation which was first calculated by Wallace [8, 9, 10], is derived from the tight-binding model [6]

$$E_{\pm}(q) \approx \pm \upsilon_F |q| + O[(q/K)^2] \tag{2.3}$$

where q is the momentum and υ_F is the Fermi velocity. $(+)$ and $(-)$ signs stand for the conduction and valence band respectively. Eq. 2.3 is the low-energy dispersion relation ($|q| \ll |K|$) and shows that the energy of charge carriers changes linearly with their momentum, not quadratically as in conventional semiconductors. Hence, low-energy carriers in graphene can be described by a Dirac-like equation which is linear in momentum rather than quadratic like the usual Schrödinger equation. This implies that around the Dirac Points, charge carriers behave like relativistic quasiparticles with zero effective mass. These so-called massless Dirac fermions move at a velocity of about $c/300$ and have a very high mobility. The experimental results show a mobility up to $15,000$ cm^2 V^{-1} s^{-1} at room temperature on a SiO_2 substrate [3, 11, 12]. The impurity scattering due to the SiO_2 substrate limits the mobility of charge carriers at this temperature, but it can be improved by suspending the graphene crystal above the silicon substrate. The reported mobility measurements on suspended samples revealed that a value $> 200,000$ cm^2 V^{-1} s^{-1} can be achieved [13, 14].

In intrinsic graphene, the Fermi level sits exactly at the Dirac point and can be shifted up (down) by doping with electrons (holes). Even though the number of charge carriers is zero at the Dirac point, graphene has a minimum conductivity thanks to its linear spectrum. Since the Dirac fermions in graphene mimics relativistic particles, they experience Klein tunneling [15], by which a relativistic particle can penetrate through a very high potential barrier with a high probability [16, 17, 18]. This tunneling results in a predicted quantum conductivity of $4e^2/\pi h$ [19, 20] and the measurements show that the conductivity of graphene is close to $4e^2/h$ at the Dirac point [21, 22].

In addition, massless Dirac Fermions in graphene behave in an unusual manner in a perpendicular magnetic field. Unlike the traditional 2D systems, graphene has a quantized Hall conductivity that is shifted by 1/2 and follows the sequence of

$$\sigma_{xy} = \pm \frac{4e^2}{h}(N + 1/2) \tag{2.4}$$

where N is the number of Landau levels [23]. This is called *half-integer* or *anomalous quantum Hall effect*, since it is neither integer nor fractional quantum Hall effect. The coefficient 4 comes from the degeneracy, since electrons have two spin states and two Dirac cones. Moreover the cyclotron energy of electrons in graphene changes with $\sqrt{B}$ which causes larger energy spacing between Landau levels. This condition makes the quantum Hall effect observable at higher temperatures, even at room temperature [24].

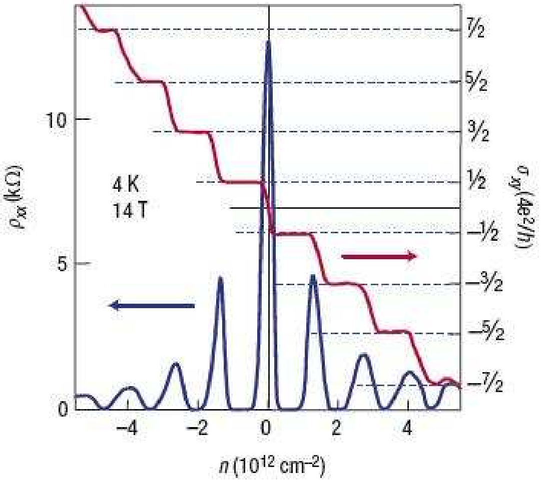

Figure 2.3: Quantum Hall Effect in graphene [3].

As for its mechanical properties, graphene has 6 phonon modes; 3 acoustic and 3 optical modes. Longitudinal and transverse acoustic modes (LA and TA) have linear dispersion relation $\omega \propto q$ and are responsible for in-plane translation and stretching of graphene. Since graphene is a 2D material sitting in 3D space, it can vibrate in the out of the plane direction. Thus graphene has also out-of-plane phonons or flexural modes. The acoustic flexural mode (ZA) energy's disperses quadratically with momentum $\omega \propto q^2$ and represents the perpendicular displacement of the graphene sheet. Phonon dispersions in graphene are shown in figure 2.4.

Due to these exceptional electronic and phononic properties, graphene can provide a very high thermal conductivity and thus is a promising candidate for thermal management in nanoscale electronics [3]. A non-contact optical measurement of thermal conductivity on graphene samples suggested that it could be up to 5×10^3 $Wm^{-1}K^{-1}$ at room temperature [25, 26]. Recent experiments [28, 29] and theoretical

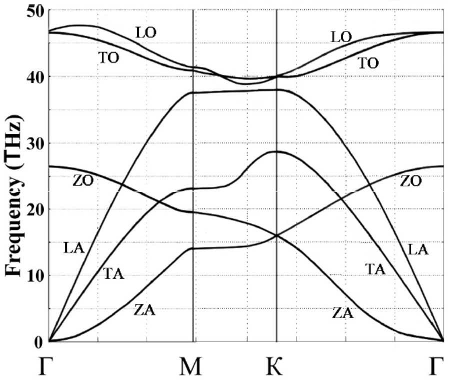

Figure 2.4: Phonon dispersions along high symmetry directions in the first Brillouin zone of graphene [27].

[30] work suggest lower values. However the experimental data is very sparse and a detailed mapping of κ remains to be done. Heat is carried by both phonons and electrons and therefore thermal conductivity of graphene has two contributions. Electronic thermal conductivity depends on the charge carrier density, whereas the phonon contribution changes with temperature.

We have introduced graphene and some of the properties that make it different from other 2DEG systems. In this project, we are interested in thermal properties and we aim to explore how heat is propagating in graphene by measuring the thermal conductivity as a function of charge carrier density and temperature. In the following sections, we present a simple theoretical model for heat transport in graphene which will later help us to analyze our measurements.

2.2 Heat Transport Model for Graphene

In this section, we present the heat transport model we use to describe our devices and analyze our data. We have two different designs for our graphene devices. We will briefly explain the design of our devices and then derive an heat equation model. We will use values from literature to estimate various material parameters and calculate a numerical estimate of the expected heat signal. The details of our device fabrication will be given in Chapter 3.

2.2.1 Joule-Heating Technique

The first device we designed has a suspended flake with two 200 nm-wide electrodes at each end (see Fig. 2.5). These narrow electrodes serve as heater and thermometer and are supported by bigger contacts for suspension. This design allows us to use Joule-heating technique. When we send a current through the thin Au wire, there will be heat generated by Joule-heating. We can calculate the power dissipated in the heater wire from its resistance and current ($P = I^2 \times R$). The input heat will flow through graphene and reach the other end where we can use the thermometer wire to measure the temperature. The temperature will be determined from the resistivity versus temperature curve for the second wire.

This device design works in theory, but in practise this design is very difficult to fabricate, especially to suspend. As you will see in the fabrication part, we need large contacts to support the graphene flake. The thin wires are not resistant to stress and

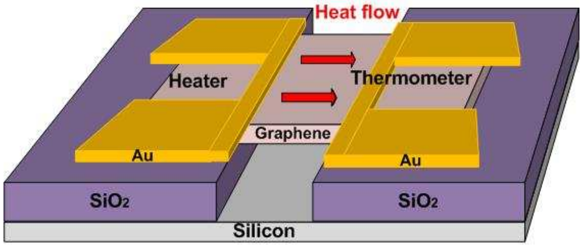

Figure 2.5: Cartoon of the device design for the Joule-heating technique.

likely to collapse. Therefore, we designed a different type of suspended device which is more suitable for suspension and developed a new heat transport model for this device configuration.

2.2.2 Self-Heating Technique

The second device design also has a suspended flake, but with 3 μm-wide electrodes (see Fig. 2.6). We make heat transport measurement by using a self-heating method. In this technique, we drive a large current which heats up the graphene and causes a hot spot in the middle of graphene flake (see Fig. 2.6). Heat will flow from the center towards the electrodes. The determination of temperature is done by resistance measurement of the graphene for $I \approx 0$. To do so, we build a calibration curve of resistance as a function of temperature. Knowing the resistance of graphene at all temperatures, we can measure the temperature change that is caused by Joule-heating ($I \neq 0$).

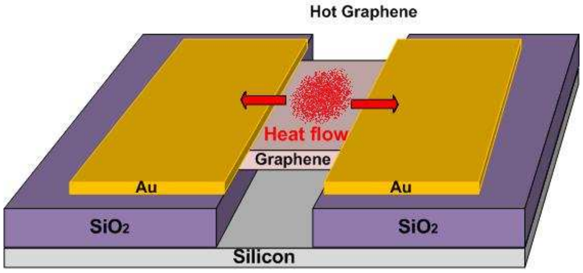

Figure 2.6: Cartoon of a self-heating device

We model this device using the general heat equation in 1-dimension:

$$\rho_m c \frac{\partial T}{\partial t} = \kappa \frac{\partial^2 T}{\partial x^2} + Q \tag{2.5}$$

where ρ_m and c are the mass density and specific heat capacity of graphene respectively. Q is the heat power per unit volume deposited in graphene, and κ is the thermal conductivity which we want to measure. When we apply a DC current, the temperature of the system will reach a steady state. Therefore, the time-dependent term is set to zero. Then, the equation reduces to

$$\kappa \frac{d^2 T}{dx^2} + Q = 0 \tag{2.6}$$

where $Q = \frac{P}{V} = \frac{I^2 R}{WLh}$ and W, L and h are width, length and thickness of graphene respectively. The 2D resistance is $R = \rho \frac{L}{W}$ and since the resistivity, ρ of graphene depends on temperature, we can substitute $\rho = \rho_{ref}[1 + \alpha(T - T_{ref})]$ where ρ_{ref} is the resistivity of graphene at a reference temperature T_{ref} and α is temperature coefficient of resistivity. Then, Equation 2.6 becomes

$$\frac{d^2T}{dx^2} + \frac{I^2\rho_{ref}}{\kappa W^2 h} + \frac{I^2\rho_{ref}\alpha T(x)}{\kappa W^2 h} - \frac{I^2\rho_{ref}\alpha T_{ref}}{\kappa W^2 h} = 0 \tag{2.7}$$

According to our model, we expect T to be maximum in the middle of the flake due to Q. While each end will be at fixed temperature set by the gold contacts which are the cryostat's temperature (see Fig 2.7).

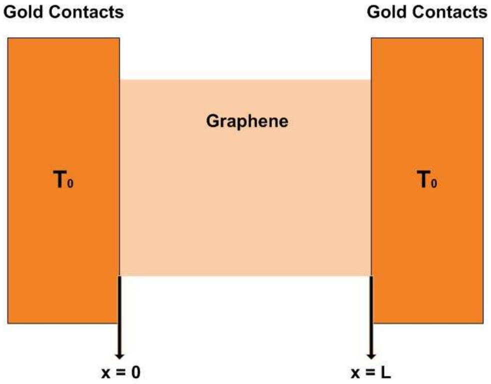

Figure 2.7: Boundary conditions for Self-heating model

Therefore, to solve Eq. 2.7 we will use the boundary conditions:

$$T(0) = T_0 \qquad , \qquad T(L) = T_0 \tag{2.8}$$

The solution is found using Mathematica or analytically:

$$T(x) = (T_0 + \frac{1}{\alpha} - T_{ref})[\cos(\sqrt{\frac{I^2\rho_{ref}\alpha}{\kappa W^2 h}}x) + \tan(\frac{L}{2}\sqrt{\frac{I^2\rho_{ref}\alpha}{\kappa W^2 h}})\sin(\sqrt{\frac{I^2\rho_{ref}\alpha}{\kappa W^2 h}}x)] - \frac{1}{\alpha} + T_{ref} \tag{2.9}$$

where κ is the thermal conductivity of graphene. Eq. 2.9 gives the temperature $T(x)$

at different points along the graphene flake from one contact ($x = 0$) to other contact ($x = L$). In this equation; L is the length of flake which is about 1 μm experimentally, W is the width which is about 1.5 μm for our devices, h is the thickness which is 0.335 nm and α is the temperature coefficient of resistivity which we extract from our ρ vs T calibration curve (α=slope of the curve divided by ρ). I is the current flowing across the flake and which we measure experimentally. Here we will substitute in different values for ρ_{ref}, κ, T_0 and I to see how the temperature distribution depends on these parameters.

Numerical analysis for $\rho_{ref} = 5000$ Ω and $\kappa = 3000\ Wm^{-1}K^{-1}$:

Here we calculate the temperature distribution along the flake assuming that the thermal conductivity of graphene is $\kappa = 3000\ Wm^{-1}K^{-1}$. The resistivity of graphene can be about as 5000 Ω in our samples close to the Dirac point. We set the reference temperature in Eq. 2.9 to $T_{ref} = 77\ K$. Substituting all these variables in Eq. 2.9 will give an equation for $T(x)$ as a function of current I, the temperature of contacts T_0 and x:

$$\begin{aligned} T(x) &= 1129.63 + (-1129.63 + T_0)\Big[\cos(1.41795 \times 10^9 \sqrt{-I^2}x) \\ &+ \tan(708.975\sqrt{-I^2}) \sin(1.41795 \times 10^9 \sqrt{-I^2}x)\Big] \end{aligned} \tag{2.10}$$

For different applied currents, we plot the graph of temperature versus x in Fig. 2.8.

For various currents, we calculate $T(x)$ for several T_0. We select currents of 1 μA, 10 μA, 100 μA, 1000 μA and contact temperatures of $T_0 = 1.5\ K$, $T_0 = 10\ K$ and $T_0 = 100\ K$. We combine the graphs of $\frac{T}{T_0}$ versus x for each current so that we can see both the effect of current and contact temperature.

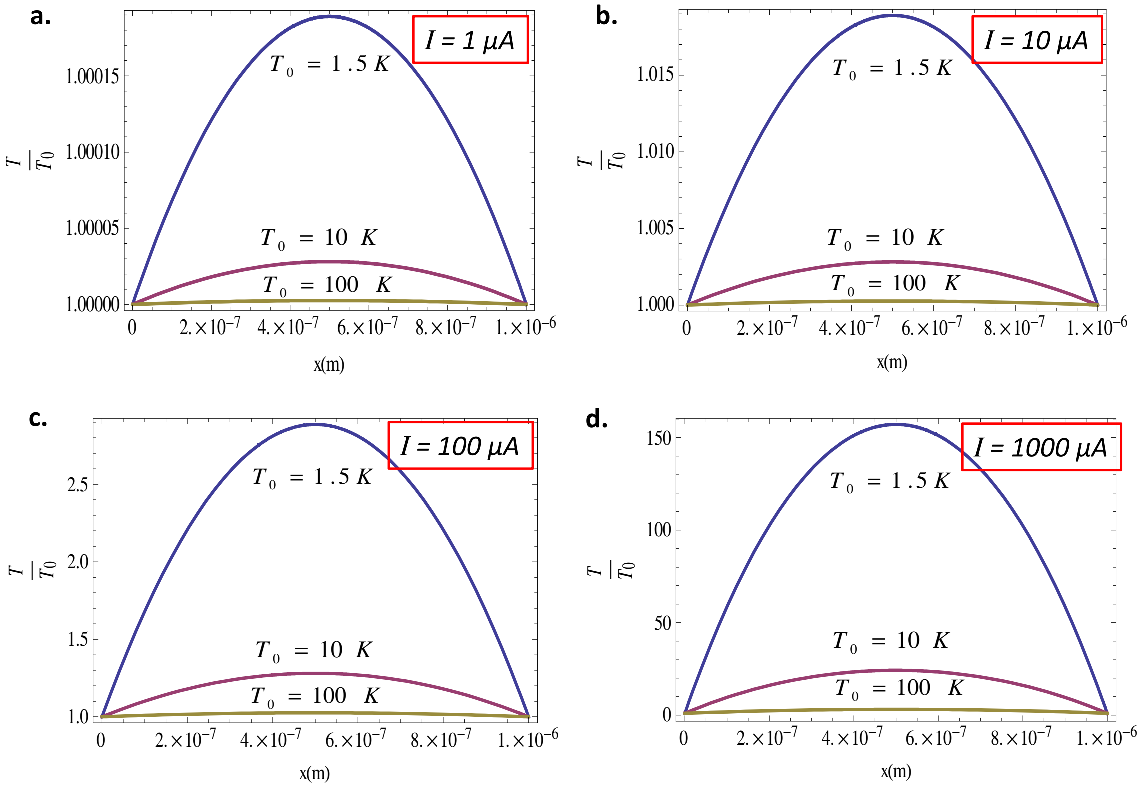

Figure 2.8: $\frac{T}{T_0}$ for $\rho_{ref} = 5000\ \Omega$ and $\kappa = 3000\ Wm^{-1}K^{-1}$. **a.** For $I = 1\ \mu A$ at contact temperatures of $T_0 = 1.5$, 10 and 100 K. **b.** For $I = 10\ \mu A$ **c.** $I = 100\ \mu A$ **d.** $I = 1000\ \mu A$.

As seen in Fig. 2.8, we get a peak temperature in the middle of the flake as we expected from our model. The hot spot in the middle results from the self-heating and the temperature goes down at the ends of the flake and reaches the temperature of the contacts. Therefore the ends sit at the ratio of $\frac{T}{T_0} = 1$. Evidently, the ratio is proportional to square of current, since the power is $P = RI^2$. Moreover, if the experiments are performed at low temperatures, the peak will be higher and thus we will have a higher signal to noise ratio.

To see the possible signal that we can detect, we calculated the temperature difference between the middle of the flake and contacts. We subtract the contact temperatures from the max points of each graph, $\Delta T = T_{middle} - T_0$, which gives the results presented in Table 2.1. Apparently a current of 1 μA is not high enough, since the difference is very small. When the current is increased, the strength of signal goes up by the square of current. At 100 μA, the different is about 3 K verifying that we get a detectable signal from our experiments. However when the current is increased further, the temperature difference blows up as seen from the result of $I = 1000\ \mu A$. This regime should be avoided since we want to measure κ at $T \approx T_0$

Table 2.1: $\Delta T = T_{middle} - T_0$ for $\rho_{ref} = 5000\ \Omega$ and $\kappa = 3000\ Wm^{-1}K^{-1}$

	$I = 1\ \mu A$	$I = 10\ \mu A$	$I = 100\ \mu A$	$I = 1000\ \mu A$
$T_0 = 1.5\ K$	$2.8 \times 10^{-4}\ K$	$2.8 \times 10^{-2}\ K$	$2.8\ K$	$234.23\ K$
$T_0 = 10\ K$	$2.8 \times 10^{-4}\ K$	$2.8 \times 10^{-2}\ K$	$2.8\ K$	$232.46\ K$
$T_0 = 100\ K$	$2.6 \times 10^{-4}\ K$	$2.6 \times 10^{-2}\ K$	$2.6\ K$	$213.78\ K$

Numerical analysis for $\rho_{ref} = 500\ \Omega$ and $\kappa = 3000\ Wm^{-1}K^{-1}$:

We would like to do the same analysis to see the difference if the resistivity of graphene is lower, which we expect when we dope the graphene using a gate electrode. For this purpose we assume the resistivity to be $\rho_{ref} = 500\ \Omega$ at room temperature and we keep the other variables the same. We substitute the parameters in Eq. 2.9, and we get the equation

$$\begin{aligned} T(x) &= 1129.63 + (-1129.63 + T_0)\Big[\cos(4.48395 \times 10^8 \sqrt{-I^2} x) \\ &+ \tan(224.198\sqrt{-I^2}) \sin(4.48395 \times 10^8 \sqrt{-I^2} x)\Big] \end{aligned} \tag{2.11}$$

We plot Eq. 2.11 using the same currents and contact temperatures as previously. The plots are shown in Fig. 2.9.

As expected, the shape of $T(x)$ is the same as earlier and the larger the current is, the higher is the temperature difference between the center and edges. We calculated the temperature difference ΔT between the middle of the flake and contacts to compare with the previous results. The results obtained are shown in Table 2.2.

Table 2.2: $\Delta T = T_{middle} - T_0$ for $\rho_{ref} = 500\ \Omega$ and $\kappa = 3000\ Wm^{-1}K^{-1}$

	$I = 1\ \mu A$	$I = 10\ \mu A$	$I = 100\ \mu A$	$I = 1000\ \mu A$
$T_0 = 1.5\ K$	$2.8 \times 10^{-5}\ K$	$2.8 \times 10^{-3}\ K$	$0.28\ K$	$27.77\ K$
$T_0 = 10\ K$	$2.8 \times 10^{-5}\ K$	$2.8 \times 10^{-3}\ K$	$0.28\ K$	$27.56\ K$
$T_0 = 100\ K$	$2.6 \times 10^{-5}\ K$	$2.6 \times 10^{-3}\ K$	$0.26\ K$	$25.35\ K$

Since we decreased the resistivity by a factor of ten, the signal also decreased by ten.

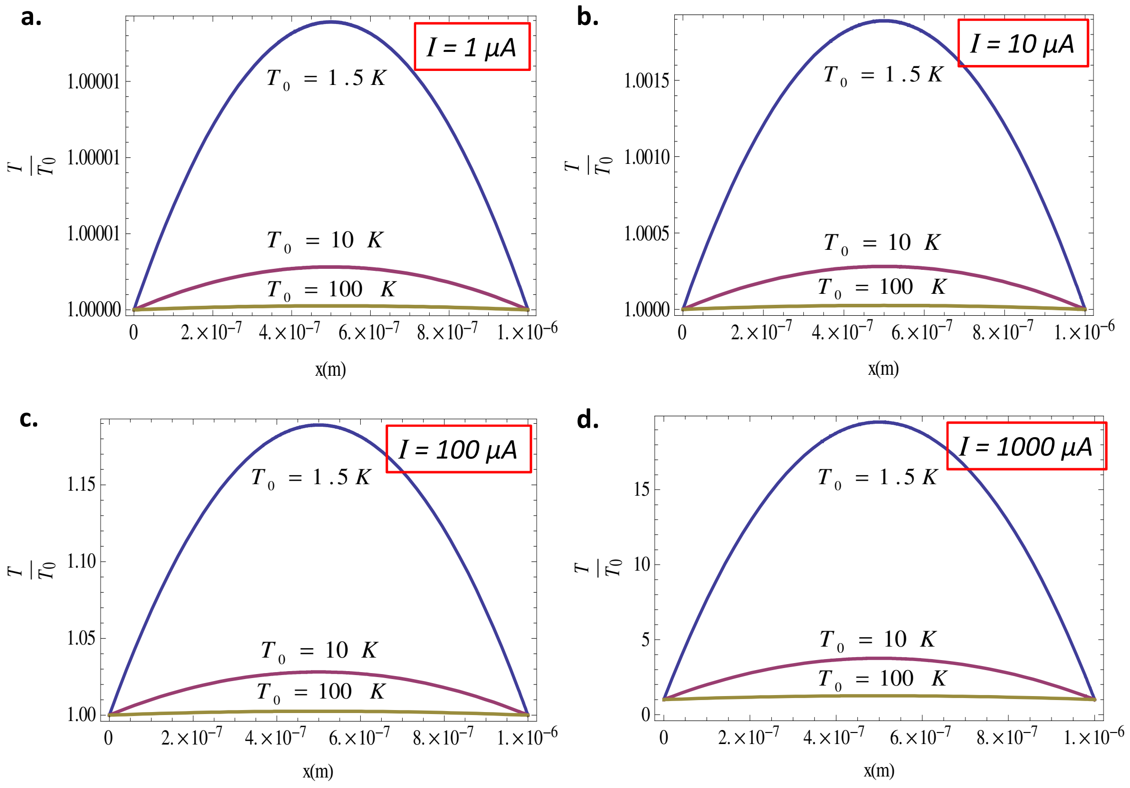

Figure 2.9: $\frac{T}{T_0}$ for $\rho_{ref} = 500\ \Omega$ and $\kappa = 3000\ Wm^{-1}K^{-1}$ **a.** For $I = 1\ \mu A$ at contact temperatures of $T_0 = 1.5$, 10 and 100 K. **b.** For $I = 10\ \mu A$ **c.** $I = 100\ \mu A$ **d.** $I = 1000\ \mu A$.

Numerical analysis for $\rho_{ref} = 5000\ \Omega$ and $\kappa = 1\ Wm^{-1}K^{-1}$:

Lastly we will study the effect of low thermal conductivity, which we expect at low temperature where there are few phonons. We assume that the thermal conductivity is much lower and we let it be $\kappa = 1\ Wm^{-1}K^{-1}$. We replace the resistivity by $\rho_1 = 5000\ \Omega$ again to compare with our first analysis. When we substitute all the parameters except for current and contact temperature, we obtain the equation

$$\begin{aligned} T(x) &= 1129.63 + (-1129.63 + T_0)\Big[\cos(7.76643\times 10^{10}\sqrt{-I^2}x) \\ &+ \tan(38832.2\sqrt{-I^2})\sin(7.76643\times 10^{10}\sqrt{-I^2}x)\Big] \end{aligned} \tag{2.12}$$

Using the same current and contact temperatures, we plot the graphs of $\frac{T}{T_0}$ vs x as seen in Fig. 2.10.

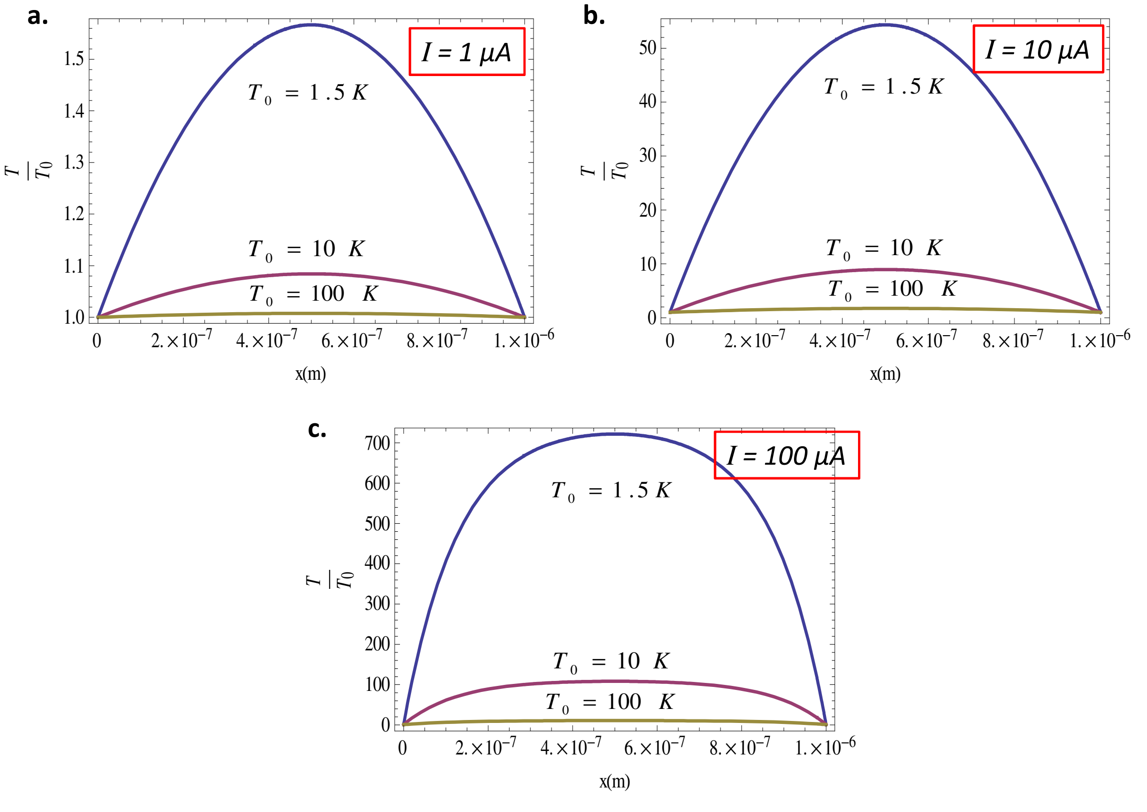

Figure 2.10: $\frac{T}{T_0}$ for $\rho_{ref} = 5000\ \Omega$ and $\kappa = 1\ Wm^{-1}K^{-1}$. **a.** For $I = 1\ \mu A$ at contact temperatures of $T_0 = 1.5$, 10 and 100 K. **b.** For $I = 10\ \mu A$ **c.** $I = 100\ \mu A$.

We calculated the temperature difference between the middle of the flake and contacts for each one. This provides us the signal range that we will have if the thermal conductivity is lower than we assumed. The results are presented in the following Table 2.3:

Table 2.3: $\Delta T = T_{middle} - T_0$ for $\rho_{ref} = 5000\ \Omega$ and $\kappa = 1\ Wm^{-1}K^{-1}$

	$I = 1\ \mu A$	$I = 10\ \mu A$	$I = 100\ \mu A$
$T_0 = 1.5\ K$	$0.85\ K$	$80.02\ K$	$1081.71\ K$
$T_0 = 10\ K$	$0.84\ K$	$79.42\ K$	$1073.56\ K$
$T_0 = 100\ K$	$0.78\ K$	$73.04\ K$	$987.26\ K$

If we compare these results with the Table 2.1, the temperature difference is higher for lower thermal conductivity. When the thermal conductivity is higher, the heat in the system is carried more easily from the center to the edges. Hence the temperature difference between the middle and contacts becomes smaller.

This section allows us to determine the temperature distribution and signal strength that we expect in our devices. The estimation of signal with different values of current, resistivity, contact temperature and thermal conductivity proves that our experiments will give a detectable signal and can be done. Since the measured resistivity of graphene is the average resistivity over the flake, the detected temperature of the flake is the average of $T(x)$. Therefore we integrate the temperature distribution function, $T(x)$ and divide by length, L:

$$T_{avg} = (T_{ref} - \frac{1}{\alpha}) + \frac{2(T_0 - T_{ref} + \frac{1}{\alpha})\tan[\frac{L}{2}\sqrt{\frac{I^2\alpha\rho_{ref}}{hW^2\kappa}}]}{L\sqrt{\frac{I^2\alpha\rho_{ref}}{hW^2\kappa}}} \tag{2.13}$$

The signal is $\Delta T_{measured} = T_{avg} - T_0$. Using Eq. 2.13, we will extract the thermal conductivity of graphene from the measured resistivity and temperature of the flake.

Chapter 3

Fabrication of Suspended Graphene Devices and Instrumentation

In this chapter we describe the microfabrication of our devices. We fabricated graphene devices in which we can make heat transport measurements. The devices are suspended so that there is no heat leakage to the substrate. We first present the fabrication techniques we used and explain each step we followed to prepare our samples. We then talk about our measurement set-up.

3.1 Sample Fabrication

In this section, we present the sample preparation techniques that we use to fabricate our devices. In Fig. 3.1 the procedure that we follow is shown and the details of each step will be explained in the following subsections.

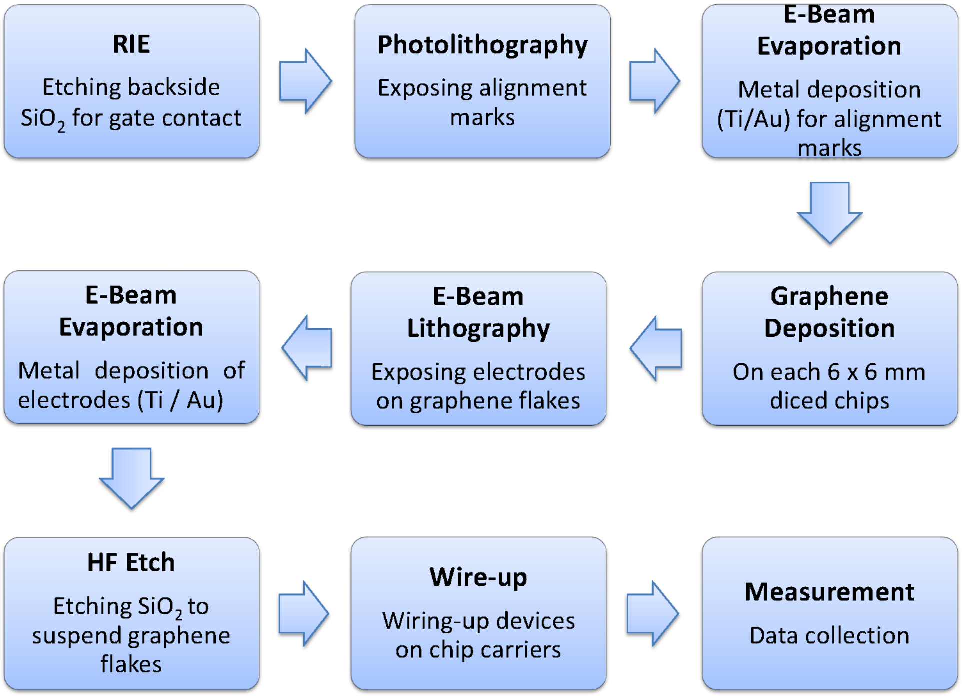

Figure 3.1: Flow-chart diagram of the fabrication of our graphene devices.

3.1.1 Reactive Ion Etching (RIE)

Throughout our work, 4-inch SiO_2 on heavily-doped Si wafers are used. First we want to remove the SiO_2 from the backside of the wafers to allow electrical connection to the Si-wafer which will be used as a gate electrode. To etch the oxide on the back of our wafers, we use RIE in which a plasma gas is accelerated between two electrodes and the ions hitting the wafer remove the oxide layer (see Fig. 3.2). The recipe we use is the following: 15 minutes at 300 W power, 100 mTorr pressure with gas flows of 22.5 sccm CHF_3 and of 2.5 sccm O_2. This etching removes completely the 300 nm of SiO_2 from the back side of the wafer. After each etching, the samples should be checked to make sure that all the oxide is etched. If not, the etch time should be increased. As Si will serve as a back-gate electrode, having SiO_2 residue on it may cause a connection problem in the measurement step. In addition, before loading wafers in the RIE chamber it is a good habit to clean wafers with N_2 gas to remove the dust. Actually, in each fabrication step I always prefer to clean my samples and the tools that I will use as much as I can. The cleanliness is extremely important for the quality of samples.

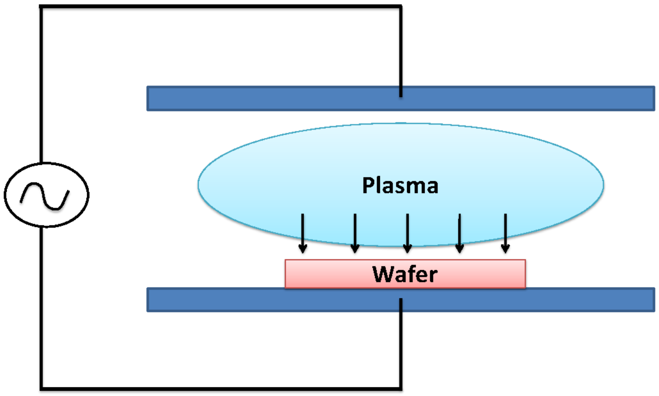

Figure 3.2: Reactive ion etching (RIE). RIE removes the SiO_2 from the backside of the wafer.

3.1.2 Photolithography

We make our devices on small chips diced from wafers. Therefore, we need a pattern on each chip to find the position of the graphene flakes and align the devices on these flakes. We use photolithography to expose alignment marks on the wafers. The mask pattern contains 15 of 15×6 mm dies and each die has an alignment mark coordinate system covering a 4×4 mm area. The pattern of alignment marks is designed as a matrix of letters (A to I) and numbers (1 to 9) with L-shapes 100 μm apart (see Fig. 3.3) The recipe that we use is the following:

1. Clean the wafers with acetone and isopropyl alcohol (IPA).
2. Spin resist S1813 at 4000 rpm for 30 seconds.
3. Bake at 115 ℃ for 60 seconds.
4. Expose for 4 seconds (depends on the intensity of light).
5. Develop with MF319 for 1 minute.
6. Rinse with DI water.
7. Inspect developed wafer. Go back to 5 if necessary.

Exposure time is set after checking the intensity of the light. We calculate the exposure time according to equation: $time \times intensity \approx 40\ mJ/cm^2$. During the developing step, we stir the beaker lightly so that the developer flows on the wafer continuously which helps to remove exposed photoresist. After developing, the wafers

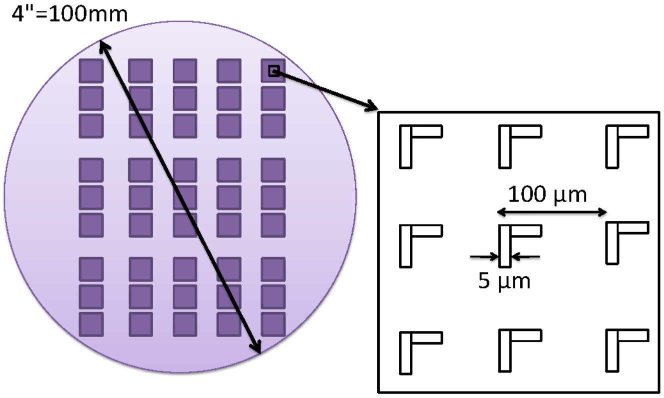

Figure 3.3: Mask Pattern and Alignment Marks. Cartoon of a 4-inch wafer with 4 × 4 mm dies with alignment marks. The inset is a zoom-in on a portion of one die and shows the dimensions of the alignment marks.

are checked under an optical microscope to make sure that there is no resist left. If not, we develop them more.

3.1.3 Electron Beam Evaporation

After developing the alignment marks, 5 nm of Titanium and 50 nm of Gold are deposited on the wafers using electron beam evaporation. The wafers are then placed for about an hour in acetone to lift-off the unexposed parts. Then the wafers are cleaned with IPA and dried. Don't forget to cover your acetone bath during lift-off, because if all of the acetone evaporates, the wafer will dry and the metal film will stick to it. If this happens, your wafer is ruined. For this reason, at any time during lift-off or if you need to move the wafer to a fresh acetone bath, never let it dry. A trick to have a fast lift-off is to use warm acetone (at about 60 ℃) and also squirting acetone on the wafer during lift-off. After a good lift-off, the wafer is ready to be diced into chips with dimensions of 5 × 5 mm. An optical image of the alignment marks on a chip is shown in Fig. 3.4.

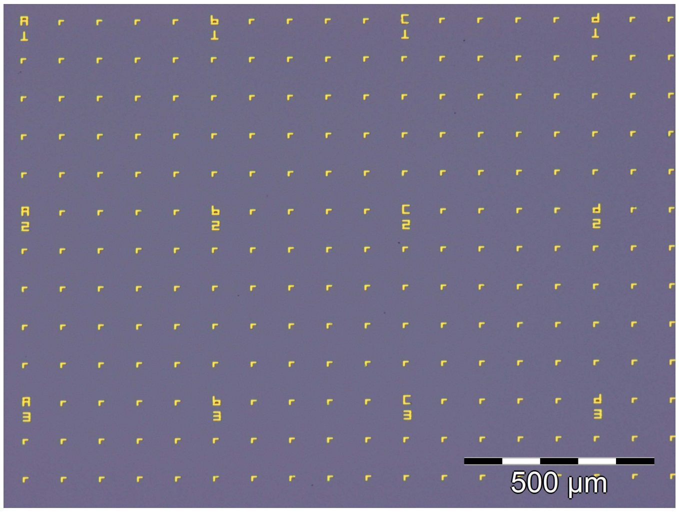

Figure 3.4: Optical image of a chip with alignment marks.

3.1.4 Graphene Deposition

Before graphene deposition, the chips are cleaned to remove any kind of contamination on them. The cleanliness between the graphene flake and the substrate is extremely important since any disorder will affect the quality of the sample and data. The recipe for chip cleaning is the following:

1. Etch for 5 minutes in a solution of $H_2O : H_2O_2 : HCl$ $(8 : 1 : 1)$ at 75 ℃.

2. Rinse with DI water and dry.

3. Bake for 2 minutes at 150 ℃ to remove water on the chip surface.

After cleaning, graphene is deposited on the chips using a scotch tape technique (or "mechanical exfoliation"). A graphite flake is attached to the sticky tape and the tape is folded and peeled apart slowly about 20 times. Each time graphite flakes are laid on a clean part of the tape in order not to shred the flakes. After enough folding, the tape is placed on chips. Using plastic tweezers, we lightly press on the tape to get rid of any air between the tape and chips for a few minutes and then we slowly peel off the tape from the oxidized surface of the chips. The graphene flakes are distinguished under an optical microscope according to the contrast between the flake and the surface of the wafer since one atom thick graphene is highly transparent. Our chips has a 300 nm SiO_2 layer which provides a good contrast due to interference of the light reflected by the graphene and the Si wafer underneath [1]. Optical images of some graphene flakes are shown in Fig. 3.5.

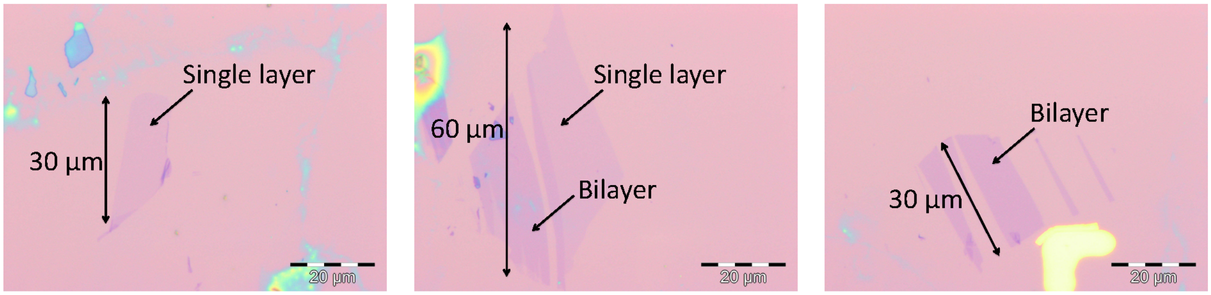

Figure 3.5: One layer and a few layers of graphene under an optical microscope with 1000x magnification.

3.1.5 Electron Beam Lithography

After locating graphene flakes during the deposition step, we can proceed to making devices. Electrodes are defined by electron beam lithography. The chips are spun and then exposed with E-beam lithography followed by a developing step. The recipe for the spinning is:

1. Spin 11% copolymer MMA at 4000 rpm for 60 seconds.
2. Bake at 170 ℃ for 15 minutes.
3. Spin 2% 950K PMMA at 2000 rpm for 60 seconds.
4. Bake 170 ℃ for 15 minutes.

After spinning the contacts are exposed on the flakes. As mentioned before, we design two kinds of devices: one with 3 μm-wide electrodes which are 1 μm apart (self-heating model) and the other one with 200 nm-wide wires at each end (joule-heating model). The contacts are drawn with an AUTOCAD program and exposed with a SEM (Scanning Electron Microscope). The procedure for making a device is shown in Fig. 3.6. After finding a flake, we put a grid on it which provides the exact position of the flake with respect to the origin at the center of four L-shapes. The contacts are drawn using the coordinate system defined by the L-shapes. During an alignment step right before exposure, the pattern is aligned using the L-shapes. After exposure, the chips are developed using this recipe:

1. Develop in MIBK : IPA (1 : 3) solution for 30 seconds.

2. Rinse with methanol for 15 seconds.

3. Rinse with IPA for 20 seconds and dry.

During each step of developing, the chips are gently stirred in the solution to help develop the exposed resist. Finally, 5 nm of Ti and 80 nm of Au are evaporated followed by a lift-off procedure (see “Electron Beam Evaporation” section for the details). As an example, the optical images of a 6-point device, used for electron transport studies, after developing and after lift-off are shown in Fig. 3.6

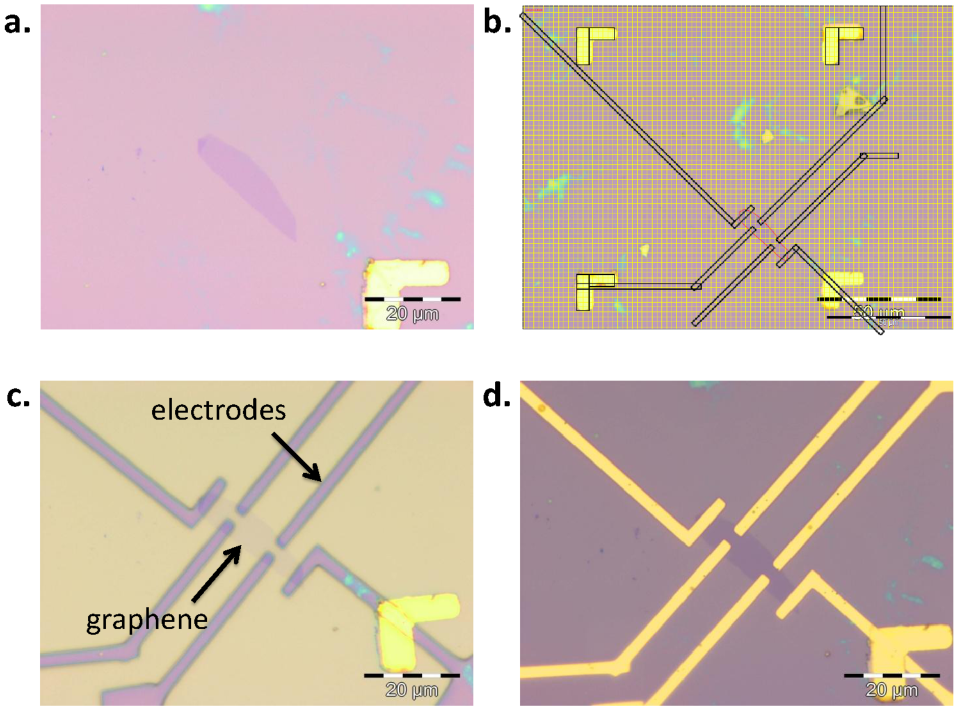

Figure 3.6: Electron-Beam lithography procedure. **a.** Optical image of a graphene flake. **b.** A grid is defined on the image to locate the flake, and the contacts are drawn by AUTOCAD. **c.** Optical image after developing e-beam pattern. **d.** Optical image after metal lift-off.

3.1.5.1 Devices for Self-heating:

Before e-beam exposure, we make a dose test to find out the right doses for the 3 μm-wide electrodes that are placed 1 μm apart from each other. In a dose test, we apply different charge doses per unit area to the same pattern to identify the optimal dose for that pattern. If you want to have sharp and small features after exposure, you must know the exact dose for each pattern. Otherwise, too low of a dose will not produce a complete pattern, and too high of a dose will result in fat shapes which will eventually cause lift-off problems. A small error in the applied dose can be improved later by developing more or sonicating during lift-off. Optical images of samples are shown in Fig. 3.7.

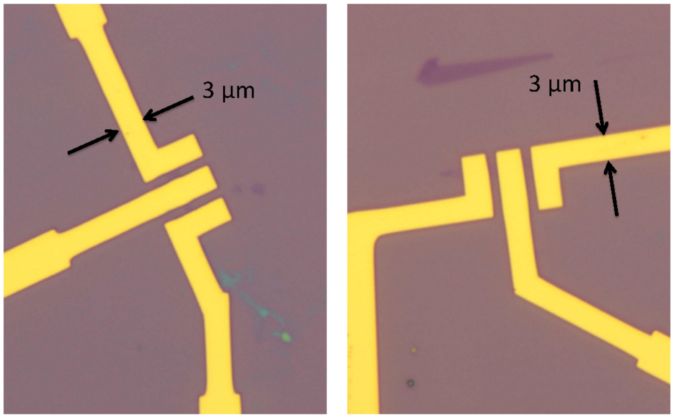

Figure 3.7: Optical images of self-heating devices.

3.1.5.2 Devices for Joule-heating:

For these devices, we start with a couple of dose tests. The doses for the 200 nm-wide wires at each end of the flake and the larger contacts that support them were verified with these tests. Then we expose our samples, evaporate and lift-off as usual. An optical image of one of our sample is shown in Fig. 3.8.

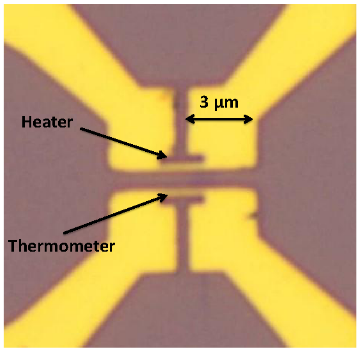

Figure 3.8: Optical image of a joule-heating device.

3.1.6 Suspension of Graphene Crystals

For the purpose of suspension, we prefer to have wide electrodes connecting the flake to increase the mechanical stability of the device. The spacing between the electrodes is set to 1 μm since shorter flakes are easier to suspend. In addition, a thicker metal film increases the rigidity of electrodes so that they will not bend during suspension.

To suspend graphene devices, we etch SiO_2 for 4 minutes with a solution of 10 : 1 $(NH_4F : HF)$. The etch rate of the solution is about 45 nm/min and so we remove about 180 nm of SiO_2. An SEM image of a suspended device is shown in Fig. 3.9.

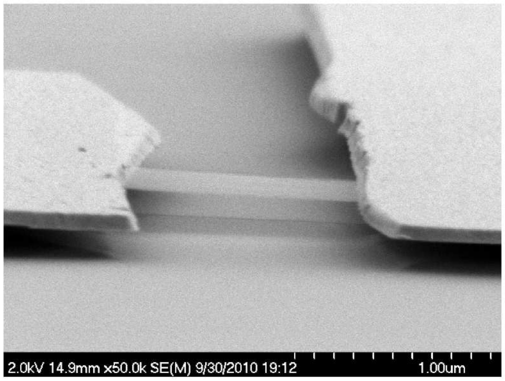

Figure 3.9: SEM image of a suspended graphene device.

For etching, the chip is immersed in the hydrofluoric acid (HF) solution and then it is rinsed in deionized water. We then rinse it in isopropyl alcohol to reduce the solvent surface tension and finally dry the chip (with N_2 gas). The most important is that while moving between solutions the chip should not be allowed to dry. Otherwise the flake will collapse on the oxide due to surface tension forces from the evaporating water. Also, it is better to keep track of the etch rate of the solution. Since the etch rate depends on temperature, it should be precisely calibrated before etching a sample.

3.2 Instrumentation

After suspending devices successfully, we are ready to prepare them for measurement. The chips are wire-bonded on chip carriers with aluminium wire. The electrodes on the sample and the back-gate electrode are connected to the pins of a chip carrier (see Fig. 3.10a.-b.). The crucial point during wire-bonding is that you should be extremely careful about electrostatic discharges. You should ground everything that is going to touch your device (like tweezers, wire-bonder, even yourself). Otherwise, the device will be destroyed.

The measurements are performed in a cryostat between 1.5 K - 420 K, where the temperature is adjusted by an external temperature controller. The cryostat has a stick with a socket at the end where we mount our chip carriers (see Fig. 3.10b.). While taking measurements, the cryostat is kept under high vacuum. It is connected with electronics which are controlled by a program we wrote with the LabWindows/CVI software. Data acquisition is also done with the same program (see Fig. 3.11).

The software can make individual bias and gate sweeps (1-D sweeps), 2-D bias and gate sweeps and also 3-D sweeps (temperature, bias and gate sweeps). It can control the entire circuit (see Fig. 3.12) and temperature of the fridge. The data is recorded to a specific directory with date and time. While recording data, the graphed data can also be seen in real time if desired. The ramping up or down parameters for the applied voltages are set at a safe rate not to destroy the samples. Thanks to this software our data acquisition is fully automated (The program was written by M.Sc. student Joshua Island).

The basics circuit for our measurement set-up is shown in Fig. 3.12. It consists of a Data Acquisition Card (DAQ) that applies bias voltage to the source electrode of the device and can also read the current from the output of a current pre-amplifier which is connected to the drain electrode. We have a gate voltage source, which is controlled

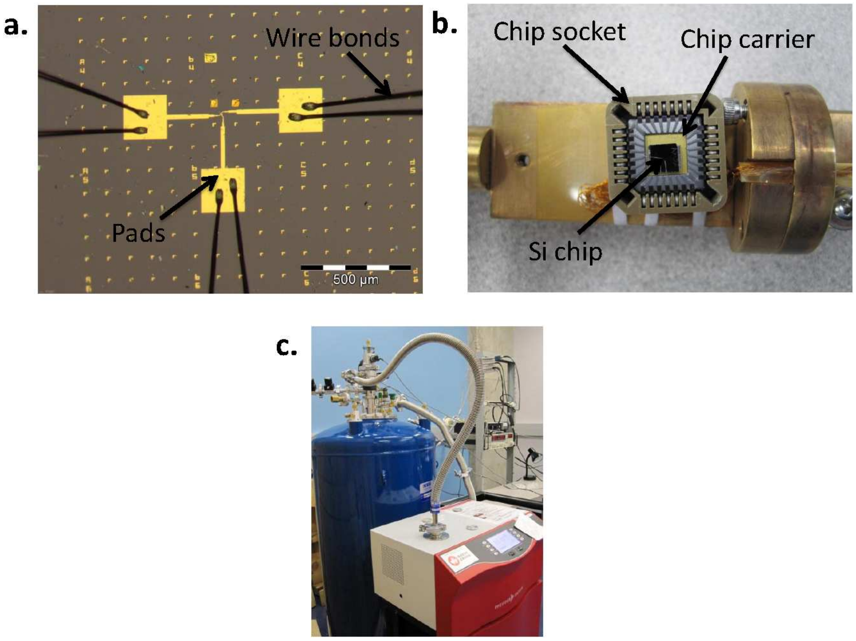

Figure 3.10: Measurement set-up an instrumentation. **a.** Optical image of a device after wire-bonding showing the large (200 × 200 μm) contact pads at the end of the source and drain electrodes. **b.** Sample mount of the cryostat with a mounted chip carrier. **c.** Cryostat connected with turbo-pump and electronics.

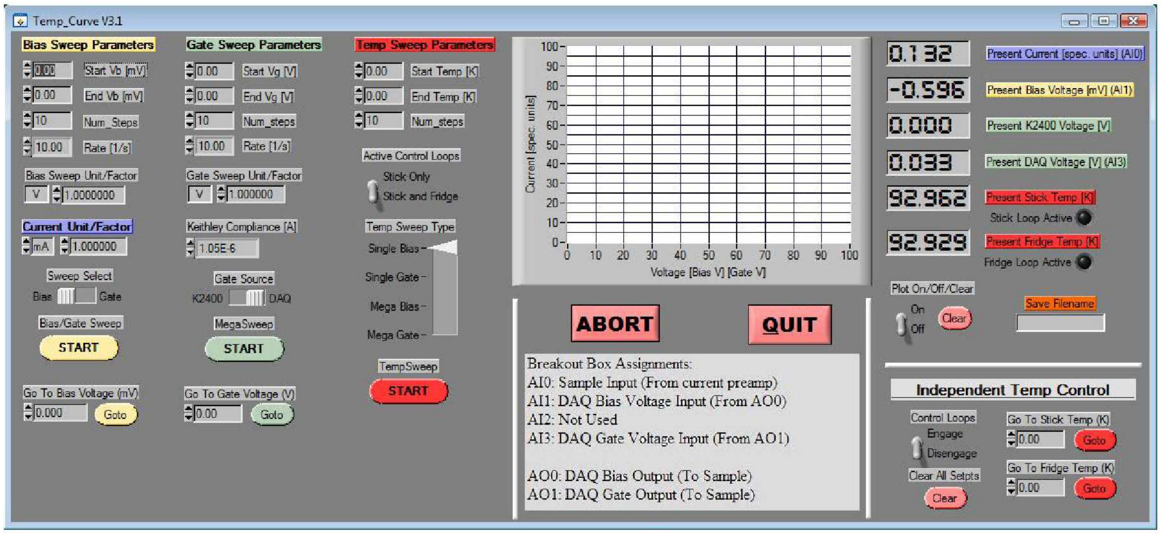

0.00 Start Vb [mV]
0.00 End Vb [mV]
10 Num_Steps
10.00 Rate [1/s]
Bias Sweep Unit/Factor V 1.0000000
Current Unit/Factor mA 1.000000
Go To Bias Voltage (mV) 0.000

0.00 Start Vg [V]
0.00 End Vg [V]
10 Num_steps
10.00 Rate [1/s]
Gate Sweep Unit/Factor V 1.000000
Keithley Compliance [A] 1.05E-6
Go To Gate Voltage (V) 0.00

0.00 Start Temp [K]
0.00 End Temp [K]
10 Num_steps

0.132 Present Current [spec. units] (AI0)
-0.596 Present Bias Voltage [mV] (AI1)
0.000 Present K2400 Voltage [V]
0.033 Present DAQ Voltage [V] (AI3)
92.962 Present Stick Temp [K]
92.929 Present Fridge Temp [K]

Go To Stick Temp (K) 0.00
Go To Fridge Temp (K) 0.00

Breakout Box Assignments:
AI0: Sample Input (From current preamp)
AI1: DAQ Bias Voltage Input (From AO0)
AI2: Not Used
AI3: DAQ Gate Voltage Input (From AO1)

AO0: DAQ Bias Output (To Sample)
AO1: DAQ Gate Output (To Sample)

Figure 3.11: The graphical interface of our home-made software for data acquisition. (coded by Joshua Island)

by GPIB via the computer, which applies a voltage to the back gate electrode of the sample to tune the charge carrier density. For all voltage sources we use either a voltage divider or a low-pass filter to reduce the noise in the circuit. For bias voltage, we prefer to use a voltage divider since the DAQ resolution is coarse for mV-range voltages. The DAQ acquires data and it is recorded by the software. A temperature controller is also connected to the PC via RS-232 and controlled by the software.

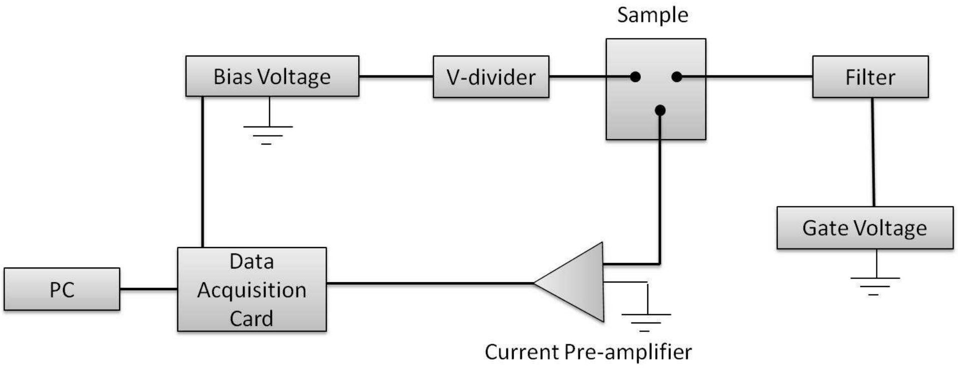

Figure 3.12: Measurement circuit. The Data Acquisition Card (DAQ) applies voltages and reads the output current from the pre-amplifier. There is gate voltage source (Keithley) which tunes the carrier density. The entire circuit is controlled by a PC.

Chapter 4

Measurements and Data analysis

After fabricating graphene transistors, we make both electron and heat transport measurements. Electron transport properties of our devices are consistent with previously reported results and prove that we fabricated high quality graphene transistors. In the first section, we present electron transport measurements and data analysis on our best suspended graphene 2 pt. device. We measured in some detail two other suspended graphene transistors and found that their qualitative behavior was very similar to the data discussed here. However, these other samples had been imaged in a scanning electron microscope prior to measurements. This reduced significantly the value of κ due to carbon contamination from the SEM. We therefore focus on our cleanest device. In the following section, we discuss heat transport measurements and the details of our results.

4.1 Electron Transport in Graphene

4.1.1 Measurements

We make two types of measurements on our samples to understand electron transport. In the first case, we sweep the bias voltage at a constant gate voltage and measure the current. Alternatively, we can sweep the gate voltage (charge density) at a constant bias voltage and measure the current. Before presenting our data analysis, let us present a representative data curve. In Fig. 4.1, we present a I versus V_{bias} sweep for different V_{gate}. Since V_{gate} tunes the carrier density, the resistance of the device changes for different V_{gate} as can be seen from the slope of different $I-V$ curves.

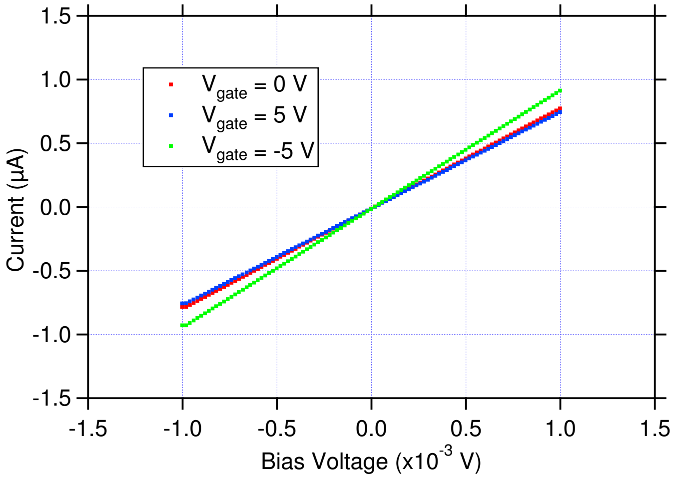

Figure 4.1: I versus V_{bias} at different V_{gate}.

For the I vs V_{gate} measurements, we sweep the gate voltage while applying a constant bias voltage for instance 5 mV. This results in a U-shaped graph (see Fig. 4.2) and the bottom of the graph shows the position of the Dirac point where the charge carrier density is zero. For intrinsic graphene, the Dirac point is at V_{gate}=0 V. However in this sample it is shifted and sits around V_{gate}=-1.3 V. This indicates that there are impurities which dope the crystal with electrons.

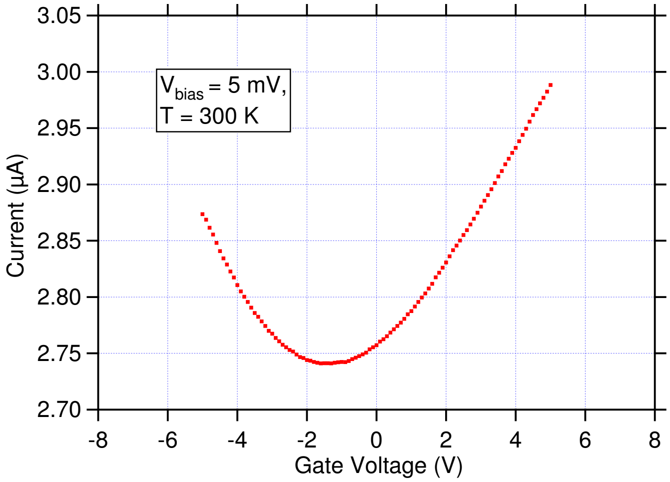

Figure 4.2: I versus V_{gate}, V_{bias}=5 mV, T=300 K.

In the following section we will give an example of electron transport data analysis procedure.

4.1.2 Data Analysis

From electron transport measurements, the first thing we can look at is the resistance of the sample. This is found by using Ohm's law. For instance, if we look at the bottom of the gate sweep graph (Fig. 4.2) where the current is 2.74 μA at $V_{gate} = V_{Dirac}$ =-1.3 V and bias voltage is 5 mV, the resistance is calculated as

$$R = \frac{V_{bias}}{I} = \frac{5\ mV}{2.74\ \mu A} = 1824\ \Omega \tag{4.1}$$

The 2D resistivity can be found from

$$\rho = R\frac{W}{L} = 1824 \times \frac{1.95\ \mu m}{1\ \mu m} = 3560\ \Omega \tag{4.2}$$

where W is the width and L the length of the graphene crystal. The electrical conductivity is the inverse of resistivity, $\sigma = 2.81 \times 10^{-4}\ \Omega^{-1} \approx \frac{7e^2}{h}$. We can also calculate the carrier density as a function of V_{gate} by using the equation

$$n = \frac{C(V_{gate} - V_{Dirac)}}{eA} \tag{4.3}$$

where C is capacitance and A is the area of the flake which is $A = 1.95\ \mu m^2$, and V_{Dirac} is the gate voltage position of the minimum of the curve in Fig. 4.2. The capacitance can be found from

$$C = \frac{\varepsilon A}{d} \tag{4.4}$$

where ε is the dielectric constant of the insulator between the gate (Si wafer) and the graphene. For our devices this insulator is vacuum, so $\varepsilon = \varepsilon_0$ and d is the distance between the gate and graphene = 300 nm. The capacitance for this device is $C = 6.5 \times 10^{-17}\ F$ and using Eq. 4.3, the carrier density at V_{gate}=0 V is found to be $n = -2.7 \times 10^{10}\ cm^{-2}$. The mobility of the charge carriers at $n = -2.7 \times 10^{10}$ cm^{-2} is found to be:

$$\mu = \frac{\sigma}{ne} \simeq 65000\ cm^2/V.s \tag{4.5}$$

The mobility is a measure of the cleanliness of our graphene, since it is proportional to the distance a charge carrier can travel without any collision. We now turn to our heat transport measurements and present an example analysis for our heat transport data to show how we extract thermal conductivity, κ.

4.2 Heat Transport in Graphene

4.2.1 Measurements

The first step for heat transport experiment is to prepare a R vs T calibration curve for each sample. This will allow us to use our device as its own thermometer. We take a current-bias voltage sweep at different temperatures (see Fig. 4.3). We sweep the voltage between -1 mV and +1 mV. By keeping the voltage range low, we make sure that there is very little Joule heating and that the temperature of flake does not change during the sweep. The slope of this graph gives the resistance of the flake at that temperature.

At several temperatures, we repeat this I vs V_{bias} sweep to find the resistance of the flake. Then we combine our results to make a resistance versus temperature graph. In Fig. 4.4, we present a sample calibration curve prepared between 79 K and 300 K. We do a fit to this curve to find the relation between resistance and

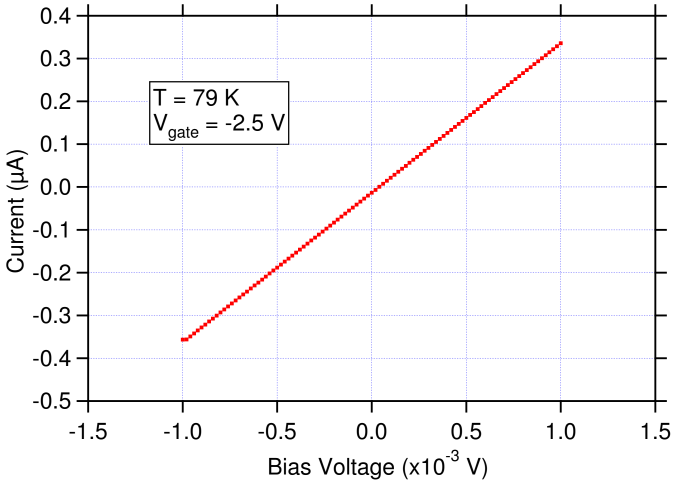

Figure 4.3: Current versus bias voltage at T=79 K.

temperature. Thus, from this relation $R = 1441 + 1947 \times e^{(-0.00523 \times T)}$ we can find the average temperature of the flake by measuring its resistance. We now have an accurate thermometer. The slope of this graph at any point is given by the derivative of the function, and corresponds to the α coefficient we use in our theoretical model (see Chapter 2). We therefore also have a measurement of α vs T.

After making a calibration curve, we are ready to perform our experiments. We apply a large bias voltage range to heat up the graphene. As seen in Fig. 4.5, at 79 K we sweep the bias voltage between -75 mV and +75 mV. The graph has a S-shape which indicates that the resistance changes and so does the temperature of the flake. For different temperatures we try different voltage ranges until we see the S-shape in graph. This confirms that our signal to noise ratio is good enough to make a precise measurement of κ.

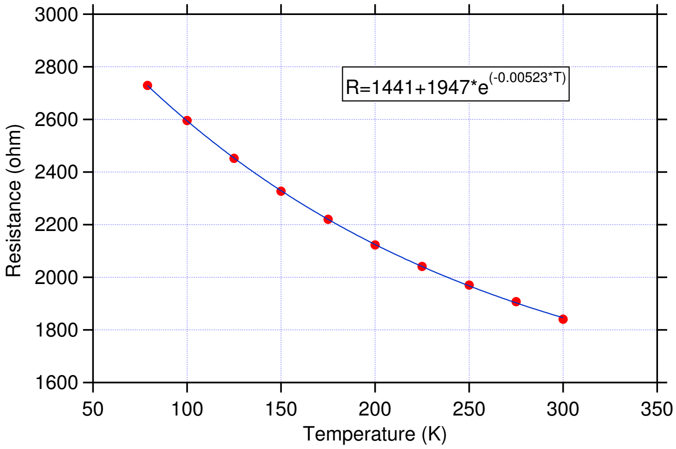

Figure 4.4: Resistance versus temperature calibration curve between 77 K and 300 K.

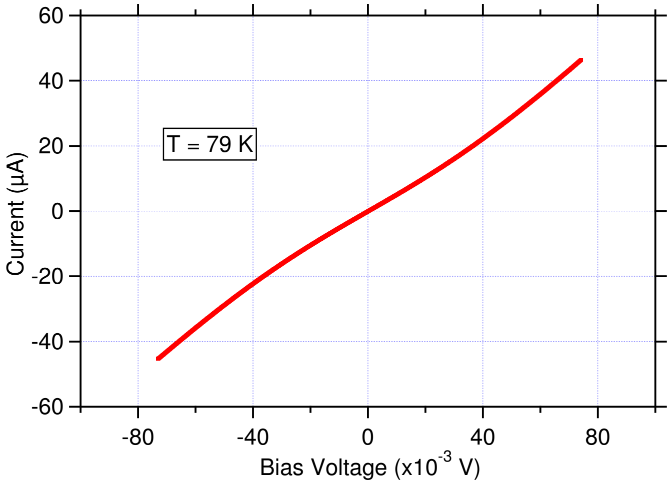

Figure 4.5: Large bias voltage sweep to heat up the graphene and measure κ.

We would like to note that for each gate voltage applied, we prepare a different calibration curve and perform a complete set of experiments.

4.2.2 Data Analysis

We are now ready to extract thermal conductivity from our data. We show an example calculation for one temperature point to explain how we calculate thermal conductivity and then we will present thermal conductivities at different temperatures. In Fig. 4.6 the R vs T calibration curve in the temperature range of 6 K - 400 K for a gate voltage of -2.5 V is shown and the points with different colors (shape) refer to different data sets taken at different times. We combine all of our data in one graph to see the behavior of resistance both at low and high temperatures.

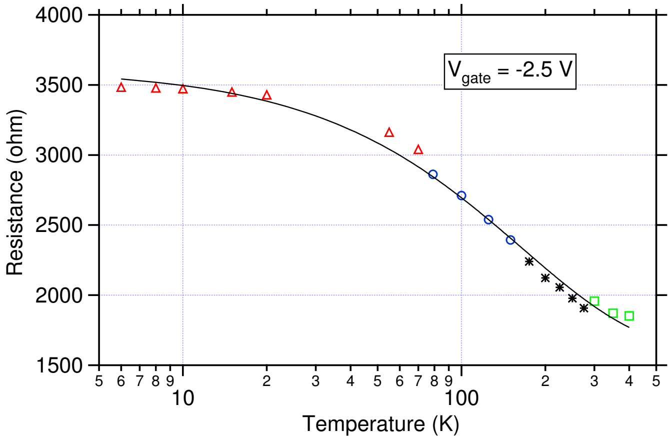

Figure 4.6: Resistance versus temperature calibration curve.

The fit for this calibration curve is

$$R = 1590 + 2025 \times e^{(-0.00606 \times T)} \tag{4.6}$$

and the temperature coefficient α is found by taking the derivative of Eq. 4.6;

$$R_{ref}\alpha = (-12.27494114) \times e^{(-0.0060614 \times T)} \tag{4.7}$$

We choose $R_{ref} = R_{measured}$ and $T = T_{average}$ in our calculations (see Eq. 2.13). Let us show how to extract thermal conductivity at $T = 350\ K$ when the applied gate voltage is -2.5 V as an example. In the experiment, we sweep the bias voltage between -525 mV and +525 mV to heat up the flake above 350 K. From our data, we pick a data point at some V_{bias} and find the resistance at that point;

$$R = \frac{V}{I} = \frac{393.5\ mV}{214.4\ \mu A} = 1835.3\ \Omega \tag{4.8}$$

To cancel any offset in the measurement, we take the corresponding point at $-V_{bias}$ on the negative side, and calculate the resistance from the average of two points:

$$R = \frac{V}{I} = \frac{-393.4\ mV}{-217.4\ \mu A} = 1809.6\ \Omega \quad , \quad R_{avg} = \frac{1835.3 + 1809.6}{2} = 1822.5\ \Omega \tag{4.9}$$

According to the calibration (Eq. 4.6), this resistance corresponds to temperature of $T = 357.1\ K$ with the signal $\Delta T = 7.1\ K$. As we did here, at each temperature T we choose a location on the $I - V$ curve where ΔT is around or lower than 10 K.

This allows us to have a well resolved $\kappa(T)$ vs T measurement. From Eq. 4.7, the temperature coefficient, $\alpha(T)$ for $R_{ref} = 1822.5\ \Omega$ and $T = 357.1\ K$ is

$$\alpha = -7.7318 \times 10^{-4}\ K^{-1} \tag{4.10}$$

In chapter 2, we build a heat transport model for our experiment and derived an expression for the average temperature of flake measured (see Eq. 2.13). If we substitute all variables into this equation and solve for κ, we get

$$\kappa = 1521\ W/m.K \tag{4.11}$$

To improve our measurements and to see the effect of impurity doping, we annealed our samples. Annealing is done by baking the samples at 420 K for a few hours. Before and after annealing we make a gate voltage sweep to see the change in the quantity of charge impurities on our sample (see Fig. 4.7) which can be seen as a change in the resistivity of the flake and a shift in the position of the Dirac point (minimum of curve).

The bottom of the curves shows that the Dirac Point is shifted by the annealing. This proves that we removed some of the impurities. We calculated thermal conductivity before and after annealing to see the dependency of thermal conductivity on the impurity level. To compare them, we plotted them on same graph as shown in Fig. 4.8.

As seen from this graph, thermal conductivity is strongly dependent on the impurity

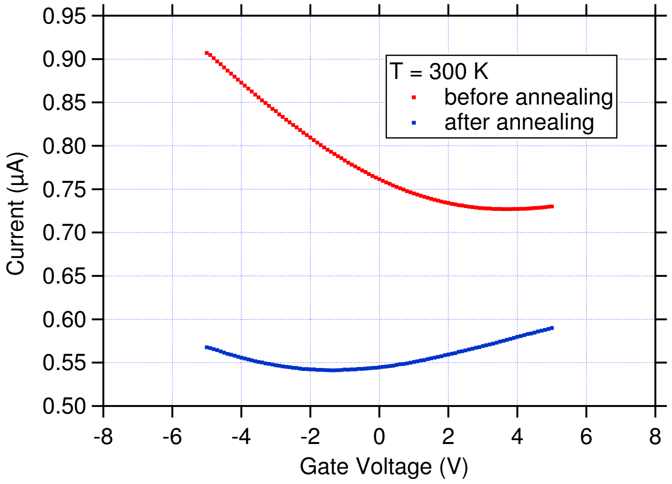

Figure 4.7: I vs V_{gate} before and after annealing.

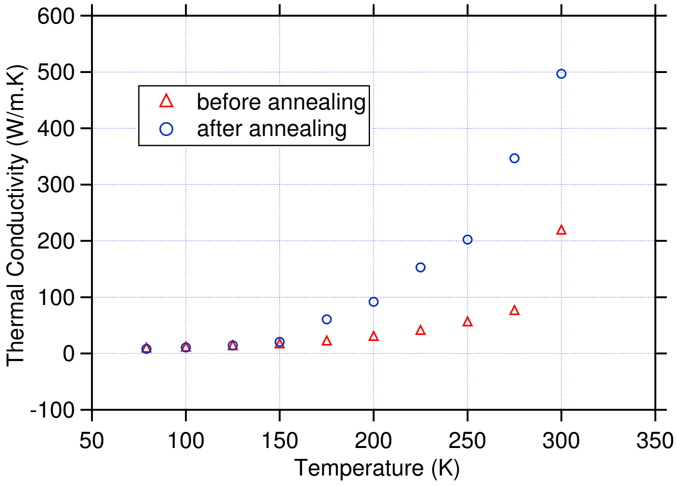

Figure 4.8: κ vs T before and after annealing.

level. After annealing, it more than doubles which indicates that with improved annealing we could reach even higher thermal conductivities.

After a long time anneal, we measured thermal conductivity as described above, versus temperature and plotted it as a function of temperature as seen in Fig. 4.9:

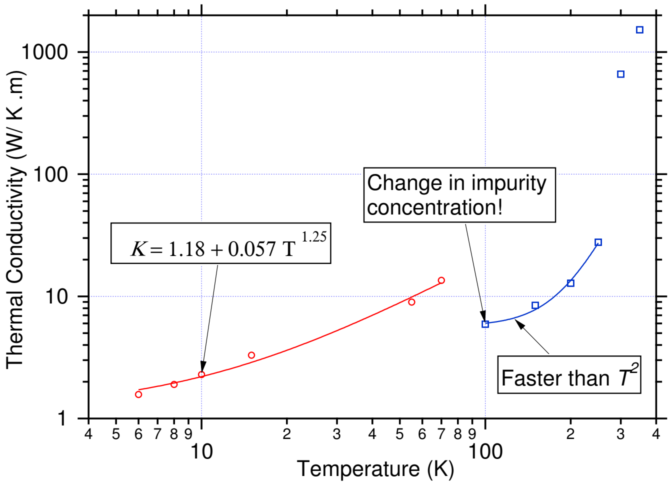

Figure 4.9: Thermal conductivity versus temperature at $V_{gate} = -2.5\ V$, which corresponds to $n_{carrier} \simeq 0.2 \times 10^{11}\ cm^{-2}$.

We also measured the thermal conductivity at different gate voltages. We plot thermal conductivity at $T = 350\ K$ as a function of V_{gate} (see Fig. 4.10).

We see a decrease in thermal conductivity with gate voltage and thus with charge carrier density. In the following section we will discuss our results and compare them with theoretical predictions and previously published results.

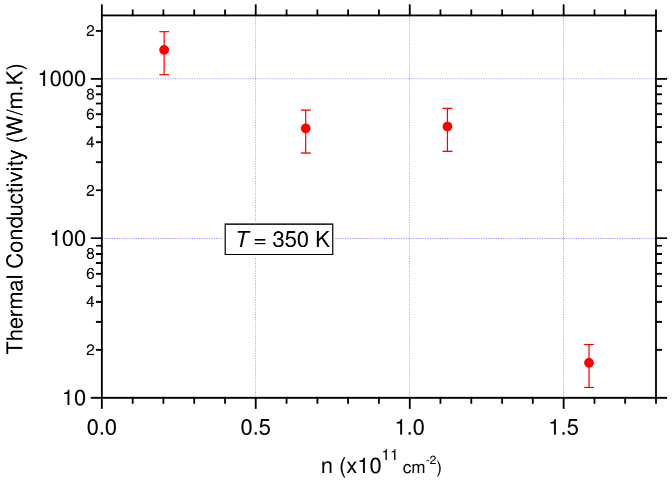

Figure 4.10: Thermal conductivity versus charge carrier density at $T = 350\ K$.

4.2.3 Discussion

Thermal conductivity has contributions both from electrons and phonons. In our samples, we have very low charge carrier densities since we do not apply large gate voltages. Therefore we expect that the thermal conductivity will be dominated by phonons:

$$\kappa = \kappa_e + \kappa_{phonon} \approx \kappa_{phonon} \tag{4.12}$$

Semi-classically κ_{phonon} can be expressed as

$$\kappa_{phonon} = \frac{1}{3} \sum_{q,s} C_{phonon} \upsilon_{phonon} l_{phonon} \tag{4.13}$$

where s is phonon branch index, $\vec{q}$ is the wave vector, C_{phonon} is specific heat capacity, υ_{phonon} is group velocity of the phonons and l_{phonon} is the phonon scattering length:

$$\frac{1}{l_{phonon}} = \frac{1}{l_{phonon-impurity}} + \frac{1}{l_{phonon-e}} + \frac{1}{l_{phonon-phonon}} \tag{4.14}$$

According to Eq. 4.14, phonons have interactions with the impurities, electrons and phonons. Phonon-phonon interaction is important at high temperatures where there is Umklapp phonon scattering, but we did not explore this regime. Hence in our system we have pre-dominantly phonon-electron and phonon-impurity interactions. The impurity density can be tuned by annealing and electron density can be tuned with the gate electrode.

The other parameters that can affect thermal conductivity are the length of flake, and its width (edge roughness). According to theoretical calculations, thermal conductivity decreases with decreasing length [27].

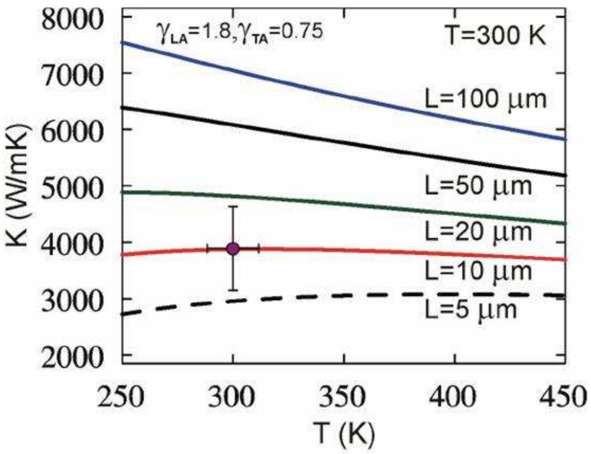

Figure 4.11: Thermal conductivity versus T for different crystal lengths [31].

.

For a 1 μm long flake, the predicted thermal conductivity is

$$\kappa \propto \frac{1}{\sqrt{L}} \approx \frac{4000}{\sqrt{L}} = 1260\ W/m.K \tag{4.15}$$

We measured thermal conductivity as $\kappa(300K) = 660 \pm 100\ W/m.K$ for a 1 μm-long flake. The discrepancy could be due to imperfect annealing and the edge roughness of the flake. The reported measurement at 300 K, $\kappa(300K) = 4000 \pm 800\ W/m.K$ [25] for a 3 μm-long flake is higher than predicted by theory and seems to be imprecise due to some poorly controlled parameters (charge density, temperature). A more recent measurement gives $\kappa(280K) = 190\ W/m.K$ [29].

For the effect of impurity density, we observed that annealing (see Fig. 4.7) reduced the impurity density by about $\triangle n_{impurity} = 7.5 \times 10^{10} cm^{-2}$ and the thermal conductivity more than doubled (Fig. 4.8). This suggest that for dirty samples phonon-impurity scattering is dominant and $l_{phonon} \approx l_{phonon-impurity}$.

The interaction between the electrons and the lattice is described by

$$\begin{aligned} H_{e-lattice} &= H_{e-lattice\ at\ rest} + H_{e-phonon} \\ &= \int dr(-e)n(r) \sum_l V_{ion}(\vec{r} - \vec{l}) \\ &- \int dr(-e)n(r) \sum_l \vec{\nabla} V_{ion}(\vec{r} - \vec{l}) \cdot \vec{y}_l \end{aligned} \tag{4.16}$$

where V_{ion} is the potential, $n(r)$ carrier density, and e is the electron charge and $\vec{l}$ is the position of ions. The electron-phonon interaction is proportional to

$n(r)$ and thus we expect that the thermal conductivity decreases with n. In our measurements, we observed that when we increase the gate voltage, thus the carrier density, thermal conductivity decreases (see Fig. **??**). This suggest that when the carrier density is increased, thermal conductivity decreases due to electron-phonon scattering. However, this measurement should be expanded for a more detailed understanding.

If we look at our thermal conductivity dependence on temperature (see Fig. 4.9), we see a more than three orders of magnitude increase with temperature. This proves that thermal conductivity is dominated by phonons as we expected. If we fit the first data set (6 K - 77 K), we get a $T^{1.25}$ dependence. The next data set (100 K - 250 K) changes with T faster than T^2. For graphene which has a quadratically dispersing out of plane phonon mode, the low temperature prediction is that $\kappa \propto T^{1.5}$ (wide flake) and $\kappa \propto T$ (narrow flake) [30]. We can see that our data is consistent with this prediction. For an infinite 2D system, it is expected that $\kappa(T) \propto C_{ph}(T) \propto T^2$. The weak T-dependence we observe at low temperatures may come from length and width of flake ($\approx 1\ \mu m$) which cut off the phonon spectrum. Also the apparent saturation of κ at $T = 350\ K$ suggests that phonon-phonon scattering is turned on due to a high number of phonons in the system.

Chapter 5

Conclusion

In this work, we designed and fabricated suspended graphene devices in which we can make heat transport measurements. We developed a self-heating technique to measure thermal conductivity by applying a current to heat up the graphene and used its resistivity as a thermometer to measure its temperature. For these measurements, we built a theoretical model by solving a steady state heat equation with the proper boundary conditions. Before starting the experiments we prepared a calibration curve (resistance versus temperature) for each sample. At each temperature, we swept a bias voltage range that is large enough to generate a good thermal signal. From our theoretical model we derived the relation between the resistivity of graphene and the average temperature of our graphene sample, and thermal conductivity was extracted by substituting the measured quantities in this model.

With our model and devices, we made the first detailed measurements of thermal conductivity in graphene as a function of temperature, charge carrier density and impurity density. We observed over 3 orders of magnitude change in resistivity under various conditions and our results ($\kappa \propto T^{1.25}$ at low-T and $\kappa = 1500\ W/m.K$ at $T = 350\ K$) are qualitatively and semi-quantitatively consistent with theoretical predictions. The dependence of κ on temperature proves that heat transport is dominated by phonons in our devices. The charge carrier density dependence of κ indicates that electron-phonon coupling also plays an important role. Annealing of our samples changes the impurity density and significantly increases their thermal conductivity.

As future prospects, we would like to measure thermal conductivity at lower temperatures to observe the thermal conductivity due to electrons. We plan to improve the annealing procedure to produce higher quality samples. As we collect more data, we expect to build a detailed understanding of electron-phonon, phonon-phonon and phonon-impurity interactions in graphene. In addition, we would like to try samples with different length and width to see the effect of flake's dimensions on thermal conductivity. Finally, we would like to learn about heat transport in the Quantum Hall regime. We will perform our experiments in high magnetic field and obtain information about the dependency of thermal conductivity on magnetic field where heat conductivity could be quantized by the presence of 1D electron edge states.

Bibliography

[1] K. S. Novoselov, A. K. Geim, S. V. Morozov, D. Jiang, Y. Zhang, S. V. Dubonos, I. V. Grigorieva, A. A. Firsov, *Science* **306**, (2004) 666-669.

[2] K. S. Novoselov, D. Jiang, F. Schedin, T. Booth, V. V. Khotkevich, S. V. Morozov, A. K. Geim, *PNAS* **102**, (2005) 10451-10453.

[3] A. K. Geim and K. S. Novoselov, *Nature Materials* **6**, (2007) 183-191.

[4] C. Lee, X. Wei, J. W. Kysar and J. Hone, *Science* **321**, 5887, (2008) 385-388.

[5] I. W. Frank, D. M. Tanenbaum, A. M. van der Zande and P. L. McEuen, *J. Vac. Sci. Technol. B*, **25**, (2007) 2558-2561.

[6] A. H. Castro Neto, F. Guinea, N. M. R. Peres, K. S. Novoselov and A. K. Geim, *Rev. Mod. Phys.* **81**, (2009) 109-162.

[7] M. Wilson, *Physics Today* **59**, (2006) 21-23.

[8] P. R. Wallace, *Phys. Rev.* **71**, (1947) 622-634.

[9] J. W. McClure, *Phys. Rev.* **108**, (1957) 612-618.

[10] J. C. Slonczewski, P. R. Weiss, *Phys. Rev.* **109**, (1958) 272-279.

[11] K. S. Novoselov, A. K. Geim, S. V. Morozov, D. Jiang, M. I. Katsnelson, I. V. Grigorieva, S. V. Dubonos, A. A. Firsov, *Nature* **438**, (2005) 197-200.

[12] Y. W. Tan, Y. Zhang, K. Bolotin, Y. Zhao, S. Adam, E. H. Hwang, S. Das Sarma, H. L. Stormer, P. Kim, *Phys. Rev. Lett.* **99**, 246803 (2007).

[13] K. I. Bolotin, K. J. Sikes, Z. Jiang, M. Klima, G. Fudenberg, J. Hone, P. Kim, H. L. Stormer, *Solid State Comm.* **146** (2008) 351-355.

[14] K. I. Bolotin, K. J. Sikes, J. Hone, H. L. Stormer, P. Kim, *Phys. Rev. Lett.* **101**, 096802 (2008).

[15] O. Klein, *Z. Phys.* **53**, (1929) 157-165.

[16] M. I. Katsnelson, K. S. Novoselov and A. K. Geim, *Nature Physics* **2**, (2006) 620-625.

[17] C. W. J. Beenakker, *Rev. Mod. Phys.* **80** (2008) 13371354.

[18] N. Stander, B. Huard, D. Goldhaber-Gordon, *Phys. Rev. Lett.* **102**, 026807 (2009).

[19] S. D. Sarma, S. Adam, E. H. Hwang and E. Rossi, *Cond. Mat.* **1003.4731v2**, (2010).

[20] J. Tworzydlo, B. Trauzettel, M. Titov, A. Rycerz, C. W. J. Beenakker, *Phys. Rev. Lett.* **96**, 246802 (2006).

[21] F. Miao, S. Wijeratne, Y. Zhang, U. C. Coskun, W. Bao, C. N. Lau, *Science* **317**, 5844, (2007) 1530-1533.

[22] R. Danneau, F. Wu, M. F. Craciun, S. Russo, M. Y. Tomi, J. Salmilehto, A. F. Morpurgo, P. J. Hakonen, *Phys. Rev. Lett.* **100**, 196802 (2008).

[23] Y. Zhang, Y. W. Tan, H. L. Stormer, P. Kim, *Nature* **438**, (2005) 201-204.

[24] K. S. Novoselov, Z. Jiang, Y. Zhang, S. V. Morozov, H. L. Stormer, U. Zeitler, J. C. Maan, G. S. Boebinger, P. Kim, A. K. Geim, *Science* **315**, 5817, (2007) 1379.

[25] A. A. Balandin, S. Ghosh, W. Bao, I. Calizo, D. Teweldebrhan, F. Miao, C. N. Lau, *Nano Lett.*, **8** (2008) 902-907.

[26] S. Ghosh, I. Calizo, D. Teweldebrhan, E. P. Pokatilov, D. L. Nika, A. A. Balandin, W. Bao, F. Miao, C. N. Lau *Appl. Phys. Lett.* **92**, 151911 (2008).

[27] D. L. Nika, E. P. Pokatilov, A. S. Askerov, A. A. Balandin, *Phys. Rev. B*, **79** 155413 (2009).

[28] S. Ghosh, W. Bao, D. L. Nika, S. Subrina, E. P. Pokatilov, C. N. Lau, A. A. Balandin, *Nature Materials* **9**, (2010) 555-558.

[29] X. Xu, Y. Wang, K. Zhang, X. Zhao, S. Bae, M. Heinrich, C. T. Bui, R. Xie, J. T. L. Thong, B. H. Hong, K. P. Loh, B. Li, B. Ozyilmaz, *Cond. Mat.* **1012.2937v1**, (2010).

[30] E. Muñoz, J. Lu, B. I. Yakobson, *Nano Lett.*, **10**, (2010) 1652-1656.

[31] D. L. Nika, S. Ghosh, E. P. Pokatilov, A. A. Balandin, *Appl. Phys. Lett.* **94** 203103 (2009).